Supporting Information

Facile one-pot generation of metal oxide/hydroxide@metal-organic framework composites: highly efficient bifunctional electrocatalysts for overall water splitting

Shasha Zheng[a], Xiaotian Guo[a], Huaiguo Xue[a], Kunming Pan[b], Chunsen Liu[c], Huan Pang[a,*]

[a]School of Chemistry and Chemical Engineering, and Institute for Innovative Materials and Energy, Yangzhou University, Yangzhou, 225009, Jiangsu, P. R. China.

[b]National Joint Engineering Research Center for Abrasion Control and Molding of Metal Materials, Henan University of Science and Technology, Luoyang 471003, China.

[c]Henan Provincial Key Laboratory of Surface & Interface Science, Zhengzhou University of Light Industry, Zhengzhou 450002, P. R. China.

*Corresponding author. E-mail: huanpangchem@hotmail.com; panghuan@yzu.edu.cn;

Content

1. Experimental section

Chemicals and Characterizations:

All chemicals, perylene-3,4,9,10-tetracarboxylic dianhydride (ptcda, 98%), cobalt acetate tetrahydrate ($Co(AC)_2 \cdot 4H_2O$), and sodium hydroxide (NaOH, 96%), were purchased from Shanghai Sinopharm Chemical Reagent Co. and used without further purification. The morphological features were characterized by field emission scanning electron microscopy (FESEM, Zeiss-Supra55), high resolution transmission electron microscopy (HRTEM, Tecnai G2 F30 S-TWIN), and energy dispersive X-ray spectrometry (EDS) mapping. X-ray diffraction (XRD) patterns were examined on a Bruker D8 Advanced X-ray Diffractometer (Cu-Kα radiation: λ = 0.15406 nm). The chemical states were measured using an Axis Ultra X-ray photoelectron spectroscope (XPS, Kratos Analytical Ltd., UK) equipped with a standard monochromatic Al-Kα source (hv = 1486.6 eV). N_2 adsorption-desorption measurements were performed on Quantachrome Instruments, Autosorb IQ3. The thermogravimetric analysis (TGA) was performed under air atmosphere with a heating rate of 5 ^{o}C/min by using a Pyris 1 TGA thermogravimetric analyzer.

Materials synthesis：

Synthesis of Co-MOF. In a typical synthesis, ptcda (0.2 mmol), NaOH (0.8 mmol), and $Co(CH_3COO)_2 \cdot 4H_2O$ (0.2 mmol) were dissolved in 35 mL deionized water with magnetic stirring at room temperature. Subsequently, the mixture was transformed into a Teflon-lined stainless steel autoclave. The autoclave was maintained at 100 °C for 12 h, and then naturally cooled to room temperature. The resulting precipitate was thoroughly washed several times with deionized water and alcohol, respectively.

Synthesis of Co_3O_4@Co-MOF. Co_3O_4@Co-MOF was synthesised using a similar procedure to that described above, except for the use of ptcda and NaOH with a mole ratio of 1 : 6. The

Co_3O_4@Co-MOF composites synthesized at reaction time of 4 h, 8 h, 12 h, and 18 h are referred to as Co_3O_4@Co-MOF-4, Co_3O_4@Co-MOF-8, Co_3O_4@Co-MOF-12, and Co_3O_4@Co-MOF-18, respectively.

Synthesis of Co_3O_4. The preparation process of Co_3O_4 was same as that of Co_3O_4@Co-MOF-12, except that ptcda is removed.

Synthesis of Co_3O_4+Co-MOF. Co_3O_4 nanocube and Co-MOF with a mole ratio of 1.5 : 1 (mass ratio of 1 : 4) were dispersed into 20 mL ethanol, and then was stirred for 30 min to form a black mixture. The obtained mixture was filtered, and dried in air naturally.

Synthesis of Ni-MOF and Fe-MOF. Ni-MOF and Fe-MOF were synthesized by a method analogous to that of Co-MOF, except that $Ni(AC)_2{\cdot}4H_2O$ and $FeSO_4{\cdot}7H_2O$ were used as the metal source, respectively.

Synthesis of $Ni(OH)_2$@Ni-MOF and Fe_2O_3@Fe-MOF. $Ni(OH)_2$@Ni-MOF and Fe_2O_3@Fe-MOF were synthesized by a method analogous to that of Co_3O_4@Co-MOF, except that $Ni(AC)_2{\cdot}4H_2O$ and $FeSO_4{\cdot}7H_2O$ were used as the metal source, respectively.

***Electrochemical Measurements*:**

Electrochemical measurements were conducted on a CHI 760e electrochemical station (CH Instruments, Shanghai, China). A conventional three-electrode system was used for the electrochemical measurements at room temperature (25 °C). A glassy carbon (GC, diameter with 3 mm) electrode coated with catalysts was used as the working electrode, an Hg/HgO electrode as the reference electrode, and graphite rod as the auxiliary electrode. The as-prepared catalysts were suspended in 1% Nafion solution (4 mg mL^{-1}). Before modification, the glassy carbon electrode (GCE, diameter with 3 mm) was polished with 0.3 μm Al_2O_3 slurry, later ultrasonic cleaning with ethanol and water. Then, 5 μL of the above suspension was added onto the GC surface and dried at room temperature. The catalyst loading density was

determined to be ≈0.28 mg cm^{-2}. All potential measurements were converted to the RHE based on the following formula $E_{vs\ RHE} = E_{vs\ Hg/HgO} + E^{\theta}_{Hg/HgO} + 0.059\times pH$. The electrochemical experiments were performed in O_2-saturated 1.0 M KOH electrolyte for OER. The HER measurements were carried in N_2-saturated 1.0 M KOH electrolyte. Linear sweep voltammetry (LSV) polarization curves were performed at a scan rate of 5 mV s^{-1} with 95% iR-compensation unless specifically indicated. Furthermore, the Tafel slope of these samples was obtained by ftting the experimental data with the equation $\eta = a+b\log|j|$, where η is the overpotential, *b* is the Tafel slope, and *j* is the current density. Electrochemical impedance spectroscopy (EIS) measurements were performed at open circuit voltage in the frequency range of 100 kHZ to 0.01 Hz in 1.0 M KOH. The overall water splitting test was performed in a two-electrode system, using two symmetric Co_3O_4@Co-MOF-12 electrodes with nickel foam as the carrier.

2. SEM images of Co_3O_4

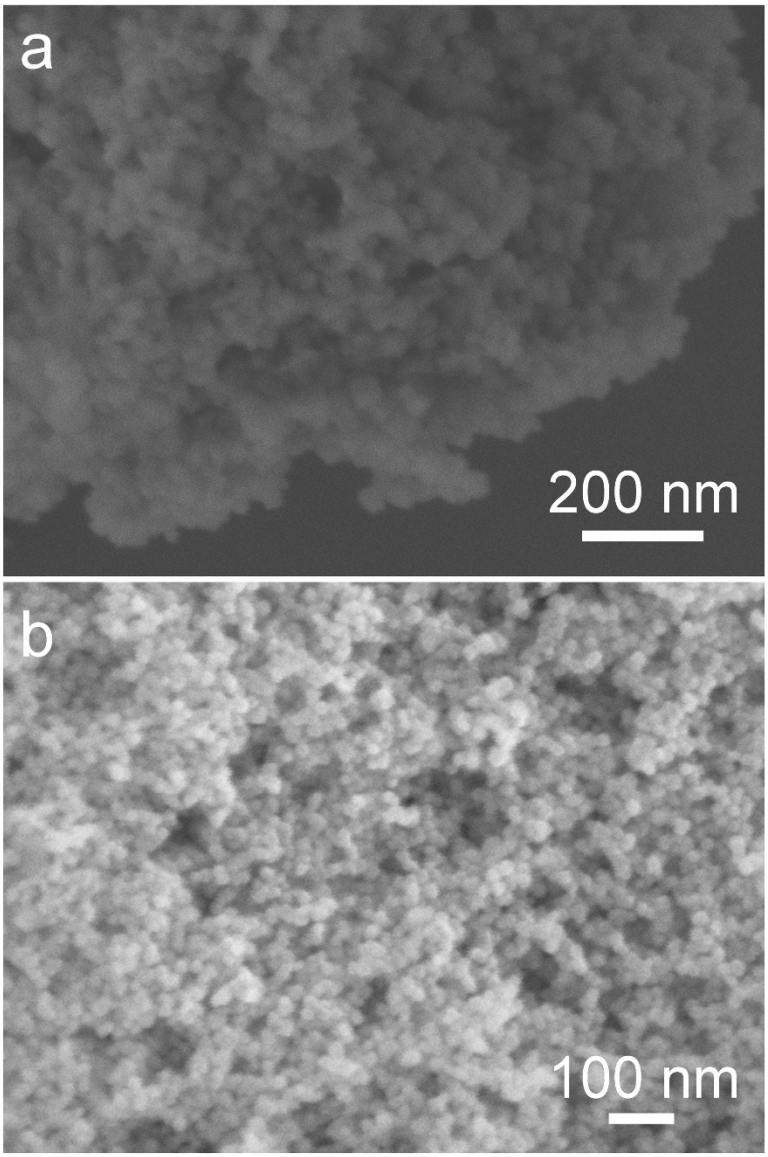

Figure S1. SEM images of Co_3O_4.

3. TG curve of Co_3O_4@Co-MOF-12

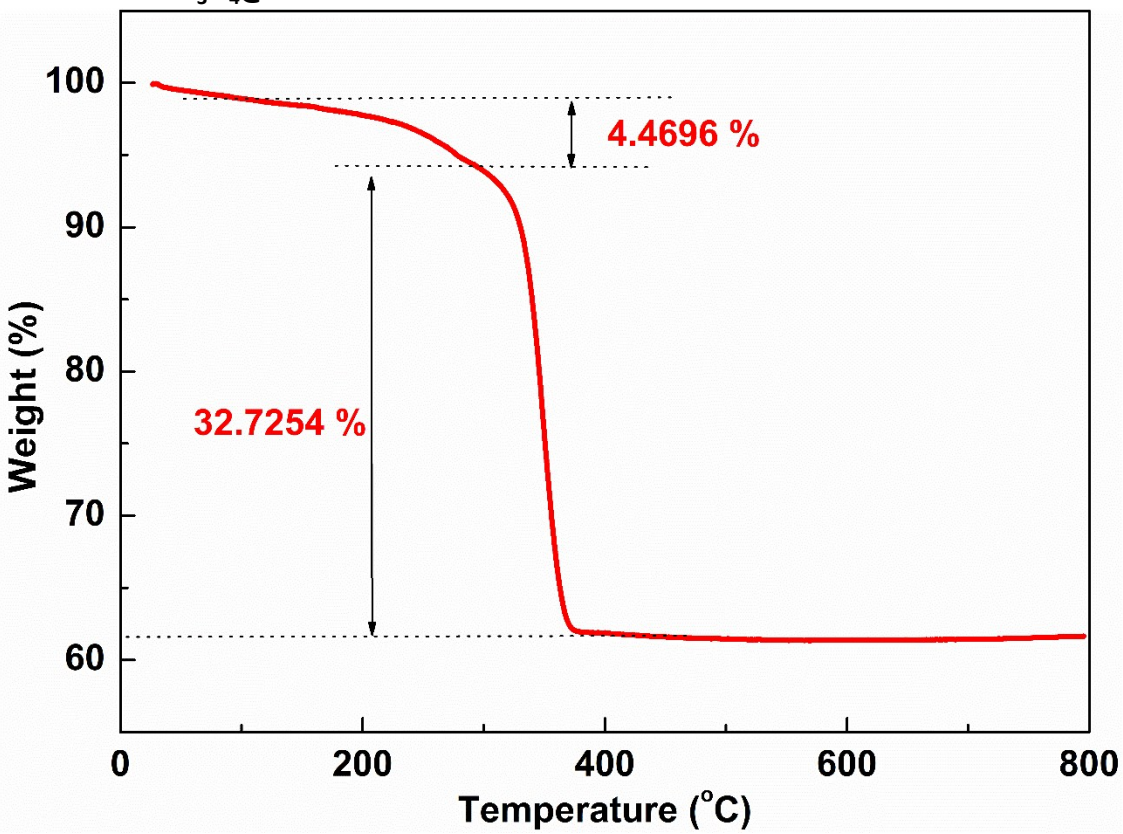

Figure S2. TG curve of Co_3O_4@Co-MOF-12.

The mass ratio of Co_3O_4 and Co-MOF in Co_3O_4@Co-MOF-12 composite was measured by TG curve. Co_3O_4@Co-MOF-12 shows very high thermal stability up to more than 300 °C. According to the TG analysis (**Figure S2**), Co_3O_4@Co-MOF-12 has two consecutive weight-loss step, at 150 and 310 °C, corresponding to the release of the coordinated water molecules (4.4696 wt%) and the loss of organic molecules (32.7254 wt%) due to decarboxylation of the ptcda ligand, respectively. The chemical reaction equations of Co_3O_4@Co-MOF-12 for two weight-loss step are as follows:

$$3Co_2(C_{12}H_4O_3)_2{\cdot}2H_2O \rightarrow 3Co_2(C_{12}H_4O_3)_2 + 6H_2O \qquad (1)$$

M	M_a = 546.2137	M_b = 510.1831	M_c = 18.0153
m	m_a	m_b	m_c
n	n_a	n_b	n_c

$$3Co_2(C_{12}H_4O_3)_2 + 76O_2 \rightarrow 2Co_3O_4 + 72CO_2 + 13H_2O \qquad (2)$$

M M_b = 510.1831 M_d = 240.7972

m m_b m_d m_e m_f

n n_b n_d n_e n_f

The known parameters:

Sample quality before testing: m_0 = 1.786 mg; coordinated water molecules, the ptcda ligand, and Co_3O_4 (including Co-MOF decomposition and Co_3O_4 from Co_3O_4@Co-MOF-12 composites, m_1) of weight percentage was 4.4696 wt%, 32.7254 wt%, and 61.6333 wt%, respectively.

$n_c = m_c/M_c = m_0 \times 4.4696\% / M_c = 0.004435$ mol

$n_b = n_a = 3/6 \times n_c = 0.0022174$ $m_b = n_b \times M_b = 1.13128$ mg

$m_e + m_f = m_b \times 32.7254\% = 0.370216$ mg

Co_3O_4 (Co-MOF decomposition):

$m_d = m_b - (m_e + m_f) = 0.76106$ mg

Co_3O_4 (Co-MOF decomposition and Co_3O_4 from Co_3O_4@Co-MOF-12 composites):

$m_1 = m_0 \times 61.6333\% = 1.10077$ mg

Co_3O_4 (from Co_3O_4@Co-MOF-12 composites):

$m_{Co3O4} = m_1 - m_d = 0.33971$ mg

Co-MOF (from Co_3O_4@Co-MOF-12 composites):

$m_a = n_a \times m_a = 1.21118$ mg

The mass/mole ratio of Co_3O_4/Co-MOF in Co_3O_4@Co-MOF-12 composites:

$m_a : m_{Co3O4} = 4 : 1$ $n_a : n_{Co3O4} = 1 : 1.5$

4. SEM image of Co_3O_4+Co-MOF

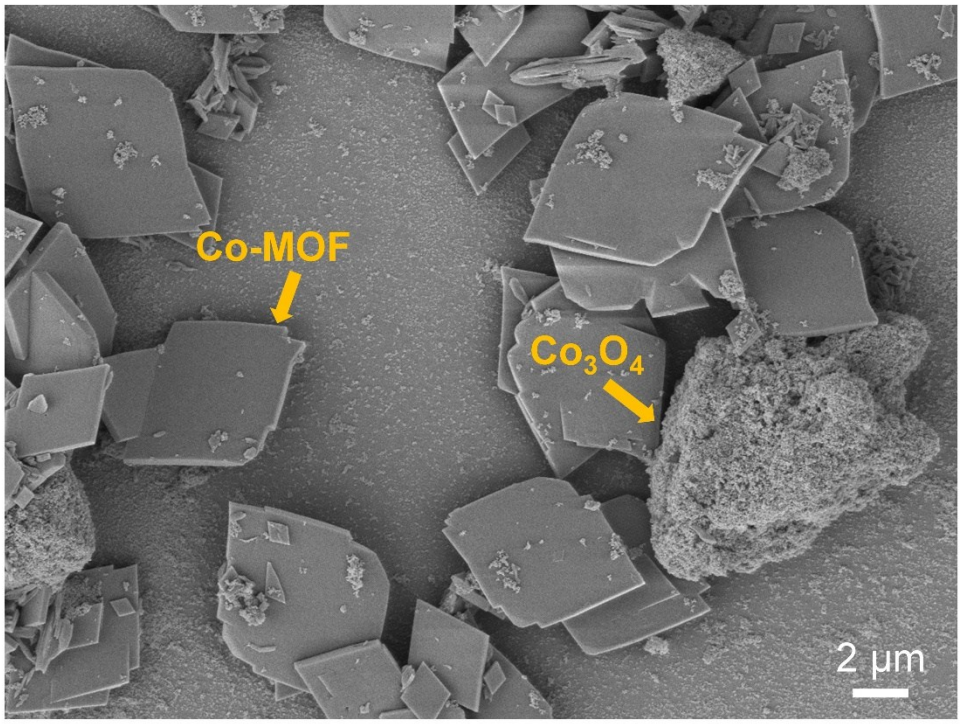

Figure S3. SEM image of Co_3O_4+Co-MOF.

5. SEM images of Co-based MOFs for different mole ratio of ptcda and NaOH

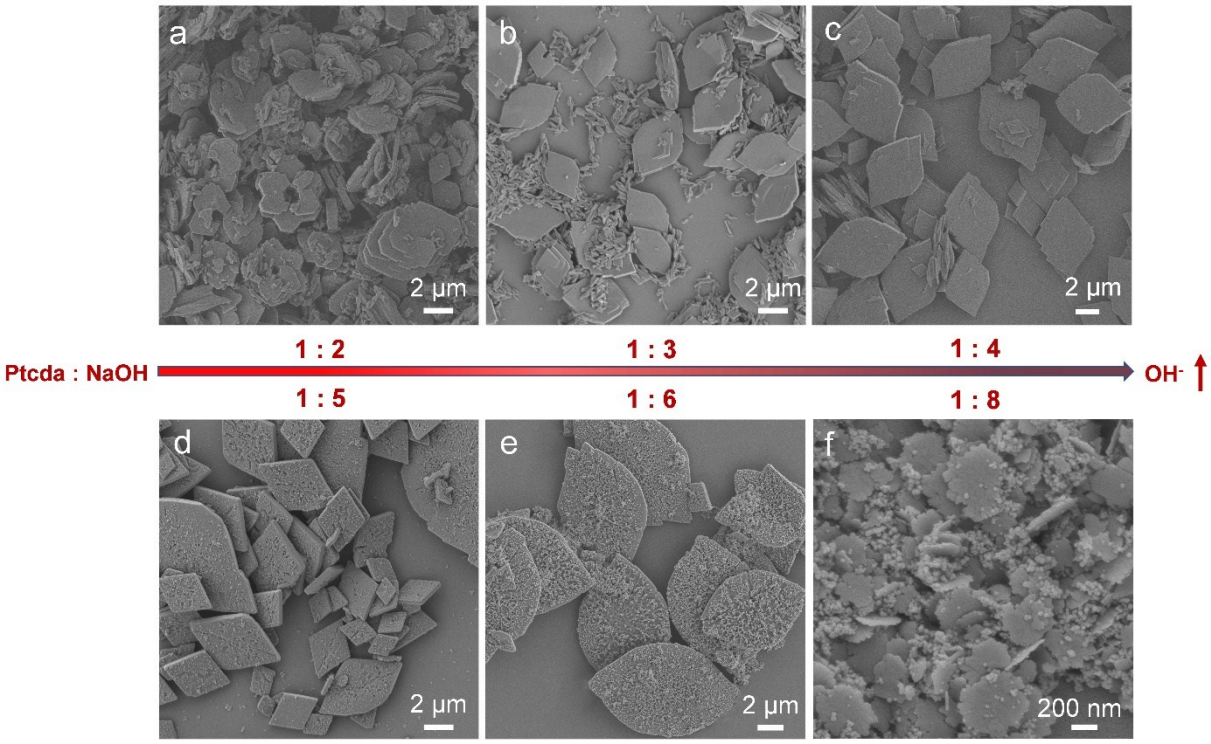

Figure S4. SEM images of Co-based MOFs obtained after hydrothermal reaction for different mole ratio of ptcda and NaOH (a) 1 : 2, (b) 1 : 3, (c) 1 : 4, (d) 1 : 5, (e) 1 : 6, and (f) 1 : 8.

In order to study the formation mechanism of Co_3O_4@Co-MOF composite, a series of Co-based MOFs were synthesised using a similar one-pot solvothermal procedure to that of Co_3O_4@Co-MOF composite, except for the use of different concentrations of NaOH solution. SEM images (**Figure S4**) show that ptcda : NaOH=1 : 2 and 1 : 3 contained the incomplete reaction ptcda. However, uniformity and sheet-like morphology Co-MOF were successfully synthesized when the mole ratio of ptcda and NaOH to 1 : 4. Subsequently, when continues to increase the concentration of NaOH, there are many Co_3O_4 nanocubes dispersed on the Co-MOF. Nevertheless, Co-MOF sheet-like morphology completely collapses when the mole ratio of ptcda and NaOH to 1 : 8. This is mainly because of the theoretical complete reaction mole ratio of ptcda and NaOH to 1 : 4, when the concentration of NaOH does not reach the ratio of complete reaction, there are some unreacted ptcda. According to the theoretical complete reaction mole ratio of ptcda and NaOH to 1 : 4, uniformity Co-MOF

were successfully obtained. As the mole ratio of ptcda and NaOH increases to 1 : 5 or 1 : 6, excess OH^- in the solution form $Co(OH)_2$ with Co(II) exposed on the surface of Co-MOF, and $Co(OH)_2$ decomposes into Co_3O_4 under hydrothermal conditions. However, continue to increase to 1 : 8, Co-MOF structure were completely destroyed. The corresponding XRD patterns (**Figure S5**) further confirmed the above the formation mechanism of Co_3O_4@Co-MOF composite.

6. XRD patterns of Co-based MOFs for different mole ratio of ptcda and NaOH

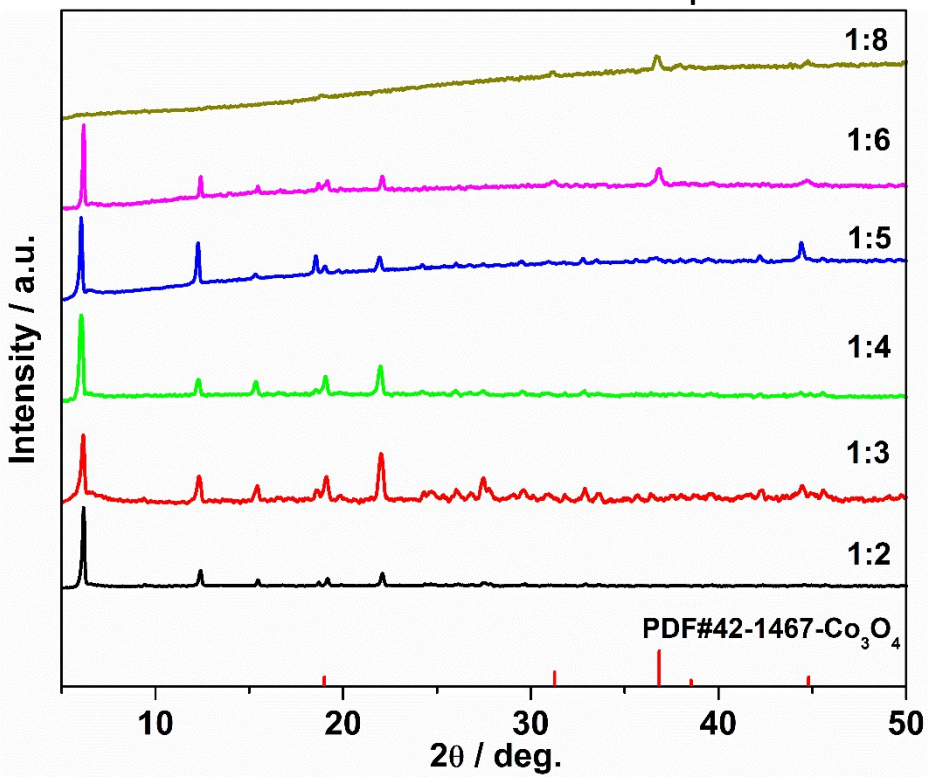

Figure S5. XRD patterns of Co-based MOFs obtained after hydrothermal reaction for different mole ratio of ptcda and NaOH.

7. SEM images of Co_3O_4@Co-MOF for different times

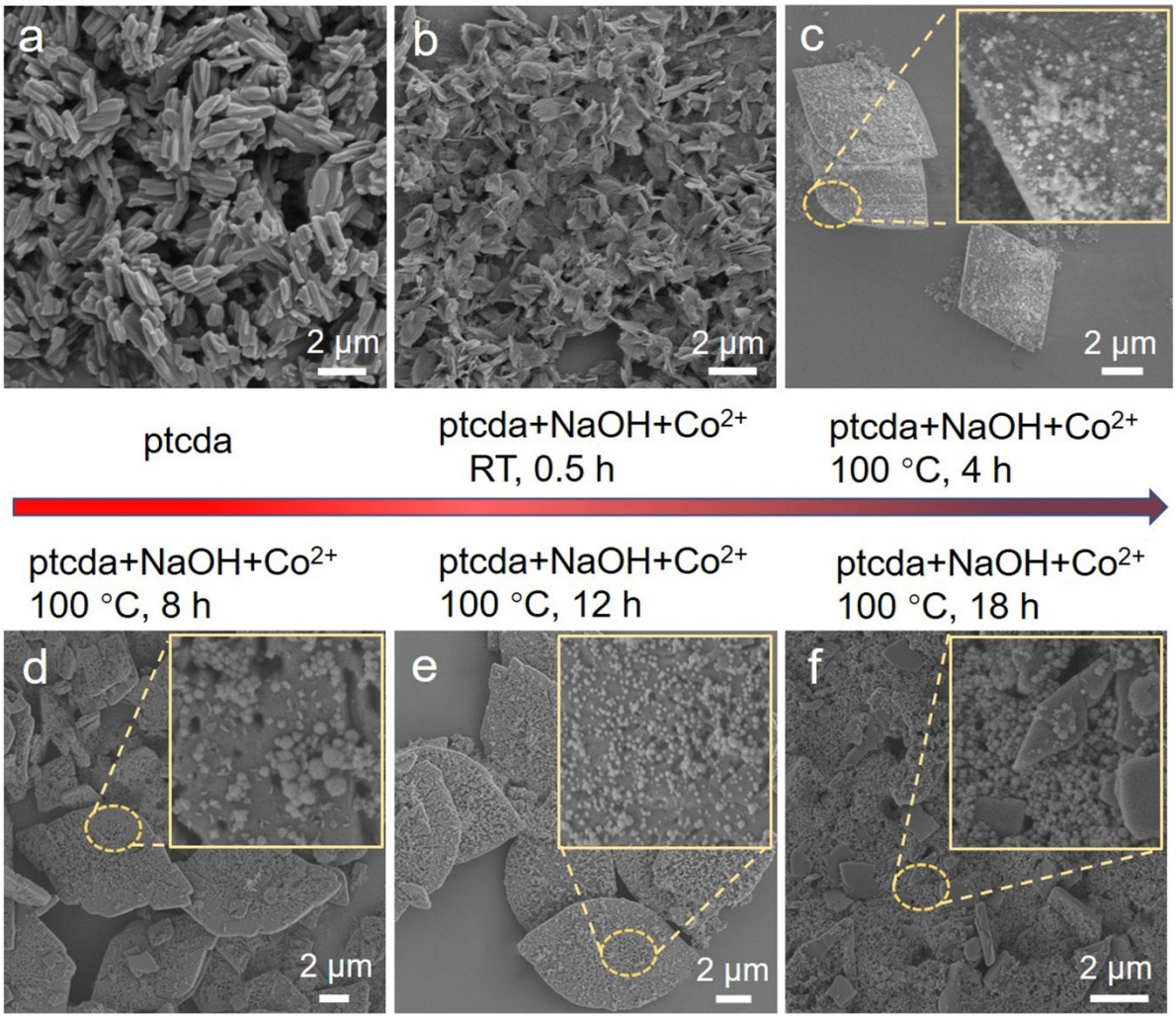

Figure S6. SEM images of Co_3O_4@Co-MOF obtained after hydrothermal reaction for different times (a) ptcda, (b) RT, 0.5 h, (c) Co_3O_4@Co-MOF-4, (d) Co_3O_4@Co-MOF-8, (e) Co_3O_4@Co-MOF-12, and (f) Co_3O_4@Co-MOF-18.

By controlling the time of reactions, we try to explore the process of Co_3O_4@Co-MOF composites growth. **Figure S6**a-f shows the SEM images of ptcda and the sample with reaction time of 0.5, 4, 8, 12, and 18 h, respectively. **Figure S7** shows the corresponding XRD patterns. As shown in **Figure S6**, the reaction time clearly affects the growth of Co_3O_4@Co-MOF composites. When the reaction time is 0.5 h at RT, there is no special morphology generated. As the reaction time is extended to 4 h at 100 ^{o}C, Co-MOF generated, and there is only very few Co_3O_4 nanocubes generated. Continuing to increase the reaction time to 12 h at 100 ^{o}C, the uniformity Co_3O_4@Co-MOF composites have been obtained, and Co_3O_4 nanocubes are

uniformly dispersed on the Co-MOF with nearly no aggregations. After 18 h, we found that Co-MOF sheet-like morphology completely collapses, and Co_3O_4 nanocubes agglomeration. Compared with other Co_3O_4@Co-MOF-t (t = 4, 8 and 18 h), the XRD peaks of the sample with reaction time of 12 h is much stronger, which demonstrates that the crystallinity becomes best.

8. XRD patterns of Co_3O_4@Co-MOF for different times

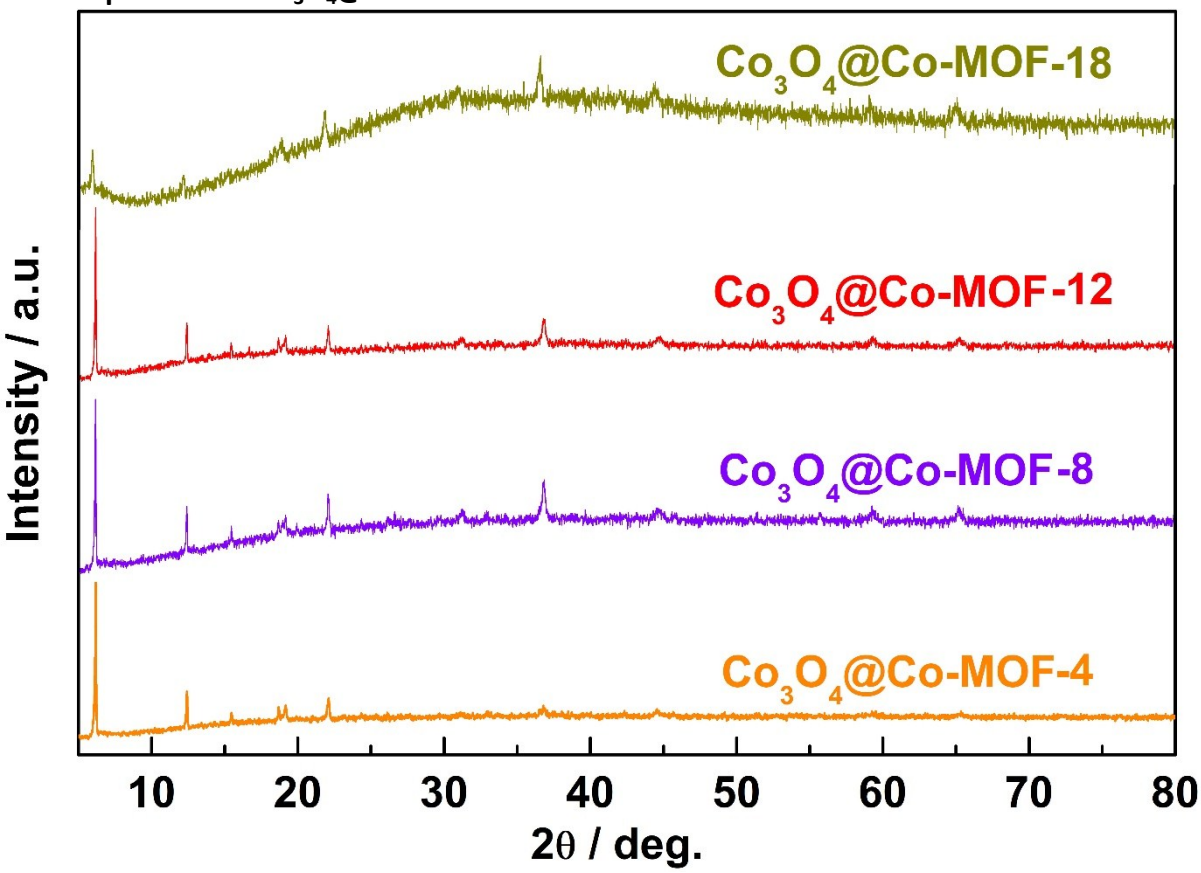

Figure S7. XRD patterns of Co_3O_4@Co-MOF-4, Co_3O_4@Co-MOF-8, Co_3O_4@Co-MOF-12, and Co_3O_4@Co-MOF-18.

9. The possible formation mechanism for the composite

The possible formation mechanism for the composite is as follows.

The reaction of the ptcda ($C_{24}H_8O_6$) and Co^{2+} in water at 100 °C for 12 h with a $C_{24}H_8O_6$:NaOH ratio of 1:4 results in a uniform Co-MOF ($Co_2C_{24}H_8O_6(OH)_4$) morphology. The following reaction occurs:

$$C_{24}H_8O_6 + 2Co^{2+} + 4OH^- = Co_2C_{24}H_8O_6(OH)_4 \quad (1)$$

Hence, the reaction equilibrium constant (K) for reaction (1) is as follows:

$$K_{MOF} = \frac{[Co_2C_{24}H_8O_6(OH)_4]}{[Co^{2+}]^2 \times [OH^-]^4 \times [C_{24}H_8O_6]}$$

As the mole ratio of ptcda and NaOH increases to 1:6, excess OH^- in the solution forms $Co(OH)_2$ with Co(II) exposed on the surface of the Co-MOF. The following reaction occurs:

$$Co_2C_{24}H_8O_6(OH)_4 + 2OH^- = [C_{24}H_8O_6(OH)_4]^{2-} + Co(OH)_2 \quad (2)$$

An equation for the overall reaction is as follows:

$$C_{24}H_8O_6 + 3Co^{2+} + 6OH^- = Co_2C_{24}H_8O_6(OH)_4 + Co(OH)_2 \quad (3)$$

Hence, the reaction equilibrium constant (K) for reaction (3) is as follows:

$$K = \frac{[Co_2C_{24}H_8O_6(OH)_4]}{[Co^{2+}]^3 \times [OH^-]^6 \times [C_{24}H_8O_6]} = \frac{[Co^{2+}]^2 \times [OH^-]^4 \times [C_{24}H_8O_6] \times K_{MOF}}{[Co^{2+}]^3 \times [OH^-]^6 \times [C_{24}H_8O_6]} = \frac{K_{MOF}}{K_{Co(OH)_2}}$$

The formation of $Co_2C_{24}H_8O_6(OH)_4 \cdot Co(OH)_2$ is caused by the different equilibrium constant K between MOF and $Co(OH)_2$. When the K_{MOF} is far greater than $K_{Co(OH)2}$, i.e., the K for reaction (3) extends far beyond 1, then the formation of $Co_2C_{24}H_8O_6(OH)_4 \cdot Co(OH)_2$ composites is more likely. In addition, $Co(OH)_2$ further decomposes into Co_3O_4 under hydrothermal conditions. By

controlling the time of the reactions, the composite obtained at 12 h (Co_3O_4@Co-MOF-12) possesses the optimal comprehensive properties, including good crystallinity, an improvement in the size/morphology uniformity and dispersion of the Co_3O_4 nanocubes. In addition, the fabrication process mentioned above can be translated to the production of other metal oxide/hydroxide@MOF composites. Ni-MOF hexagonal prisms (**Figure 2**e,f) and Fe-MOF nanobelts (**Figure 2**i,j) were successfully prepared at pH=6-8. At pH=11-13, $Ni(OH)_2$ nanosheet@Ni-MOF hexagonal prism ($Ni(OH)_2$@Ni-MOF, **Figure 2**g,h) and Fe_2O_3 nanoparticle@Fe-MOF nanobelt (Fe_2O_3@Fe-MOF, **Figure 2**k,l) composites were obtained. XRD patterns further verified the successful preparation of $Ni(OH)_2$@Ni-MOF and Fe_2O_3@Fe-MOF composites (**Figures S8,9**).

10. XRD patterns of Ni-MOF and $Ni(OH)_2$@Ni-MOF

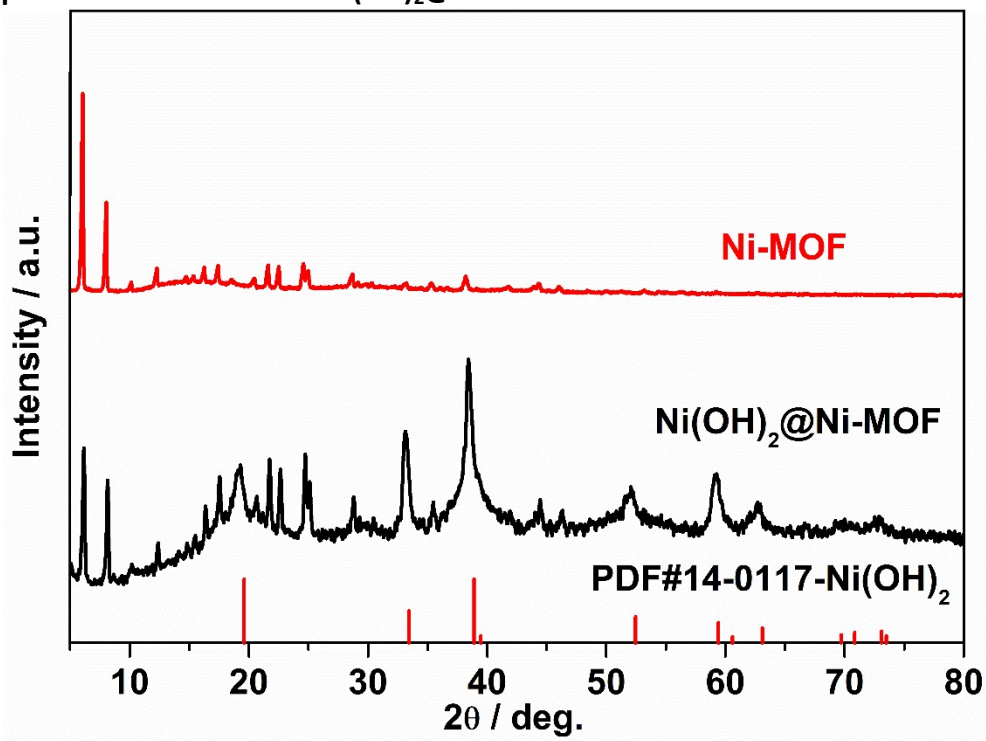

Figure S8. XRD patterns of Ni-MOF and $Ni(OH)_2$@Ni-MOF.

11. XRD patterns of Fe-MOF and Fe_2O_3@Fe-MOF

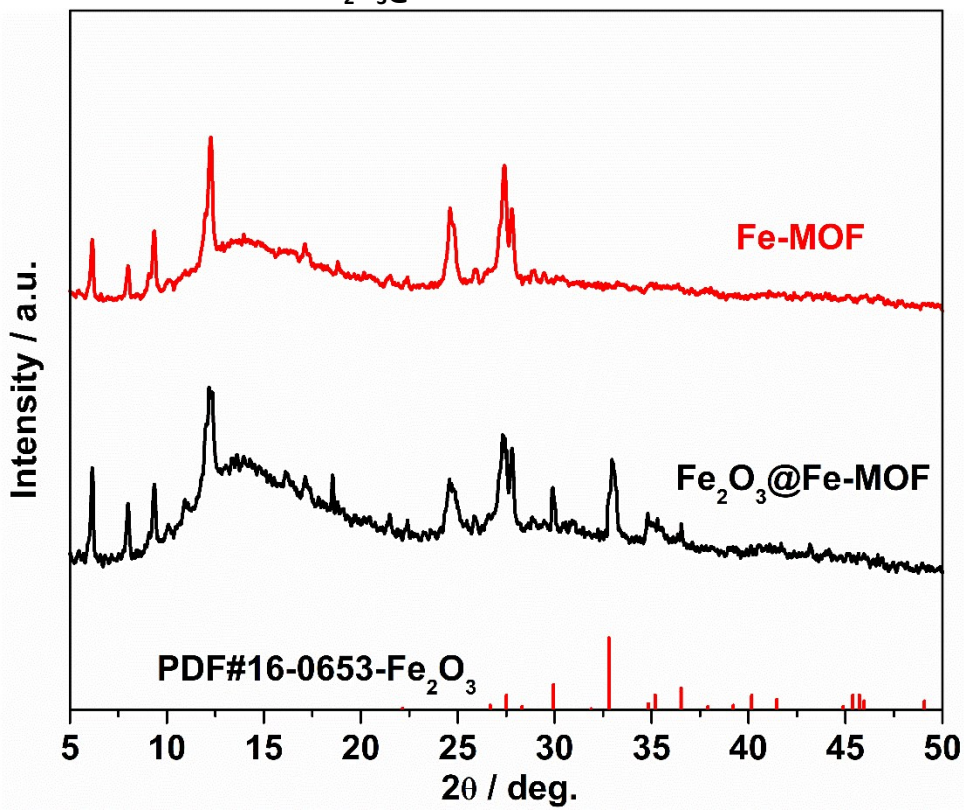

Figure S9. XRD patterns of Fe-MOF and Fe_2O_3@Fe-MOF.

12. IR pattern

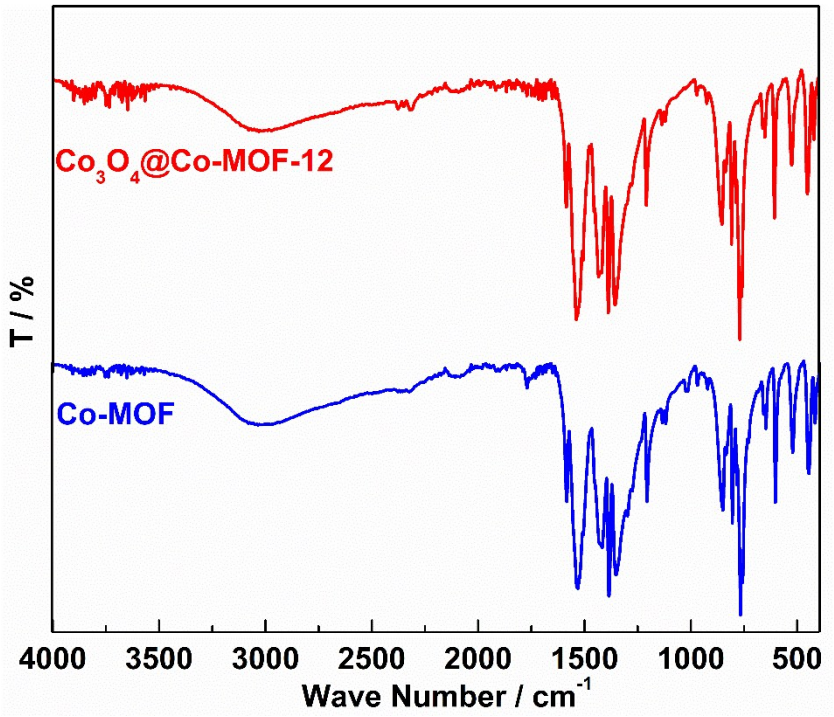

Figure S10. IR pattern of Co-MOF, and Co_3O_4@Co-MOF.

The Fourier transform infrared (FTIR) spectra of the Co-MOF-based materials are displayed in **Figure S10**. After the reaction of Co^{2+} with ptcda, the typical C=O stretching vibrations (1772, 1755, 1741, and 1730 cm^{-1}) disappear, and a new strong band at 1535 cm^{-1} appears, corresponding to the anti-symmetric stretching vibration of –COO–, confirming the successful coordination of the carboxyl groups to Co^{2+}.

13. XRD pattern of Co_3O_4

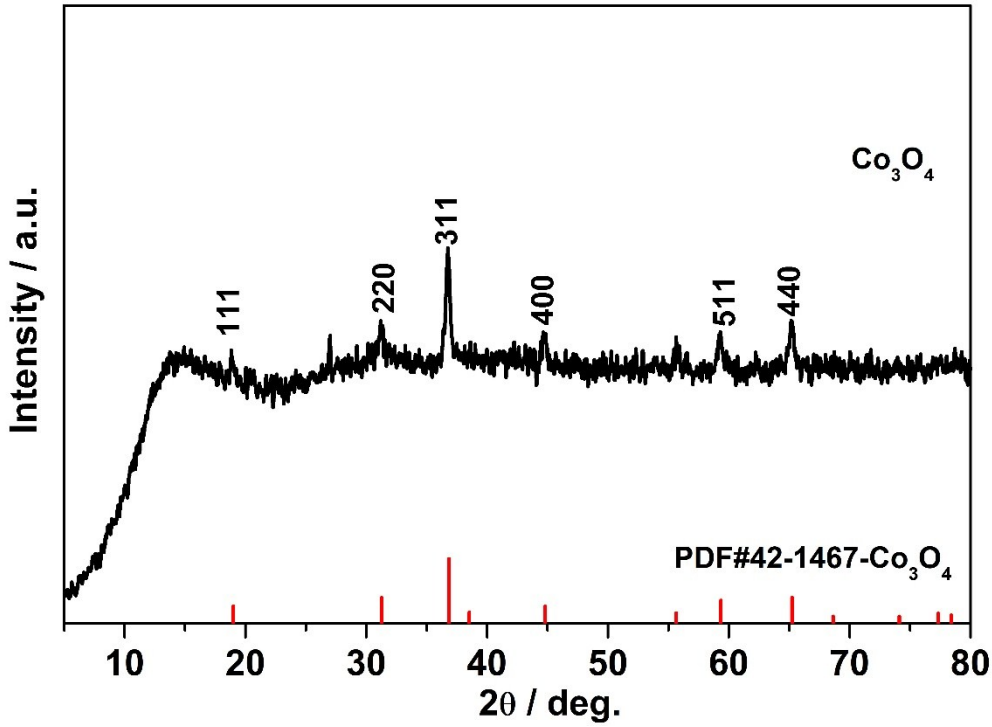

Figure S11. XRD pattern of Co_3O_4.

14. XRD pattern of Co_3O_4+Co-MOF

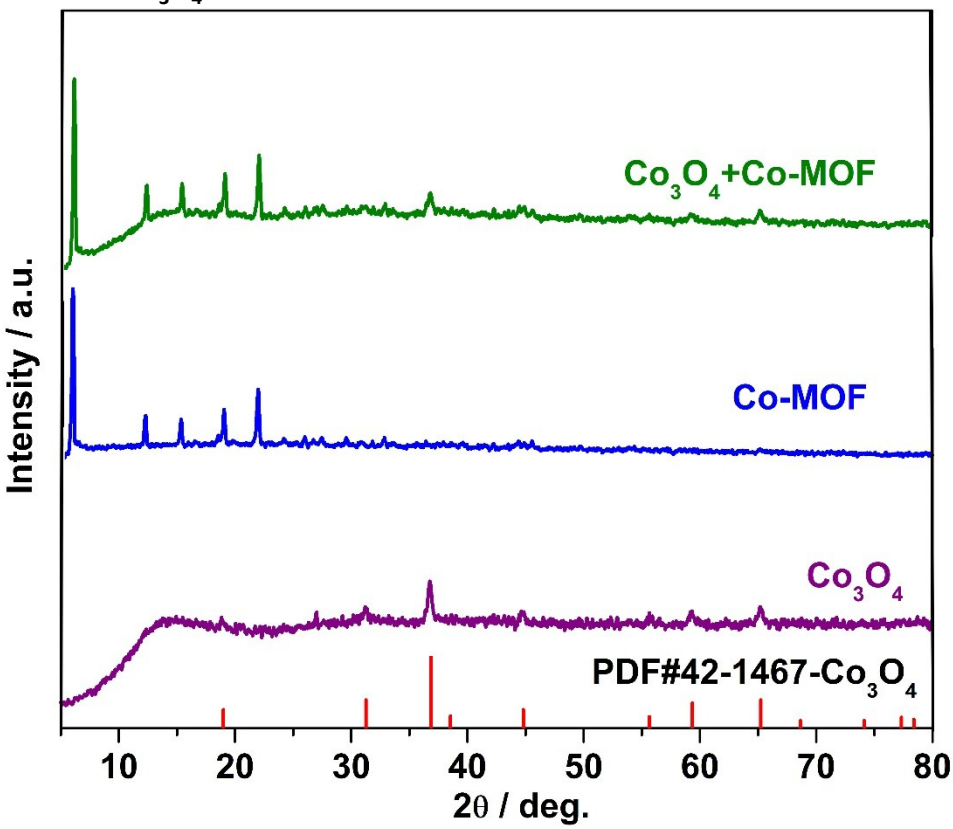

Figure S12. XRD pattern of Co_3O_4+Co-MOF

15. XPS spectra of the Co 2p

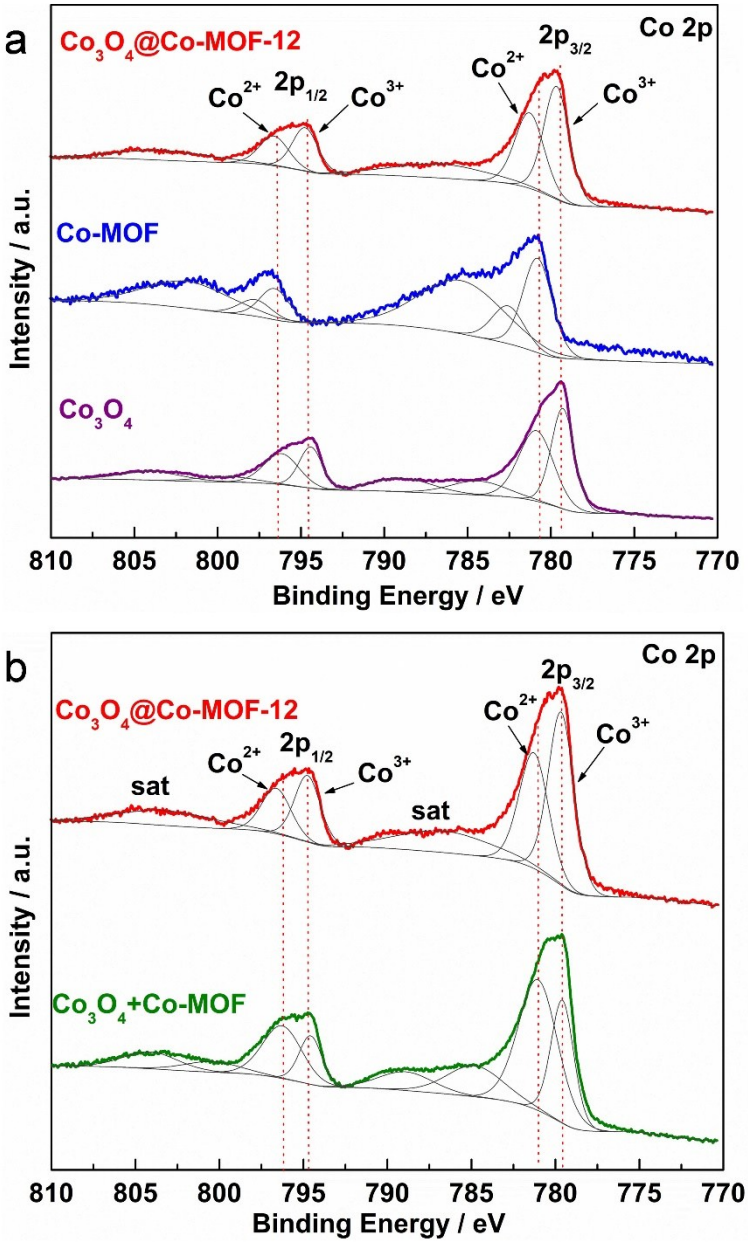

Figure S13. XPS spectra of the Co 2p

16. XPS spectra

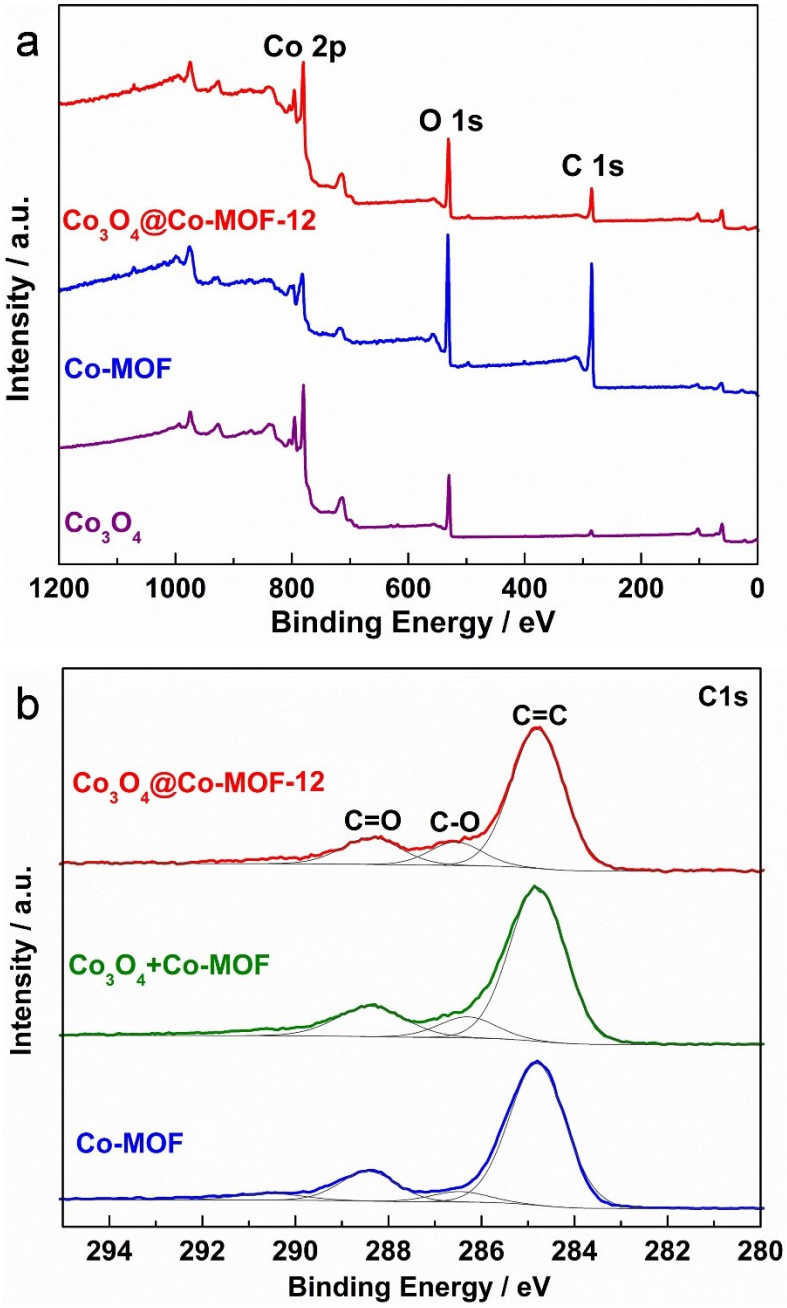

Figure S14. XPS spectra

The C 1s XPS spectra are shown in **Figure S14**b. The possible presence of C=O (288.1 eV), C-O (286.2 eV), and C=C (284.6 eV) species in the C 1s spectrum is shown.

17. XPS spectra of the O 1s

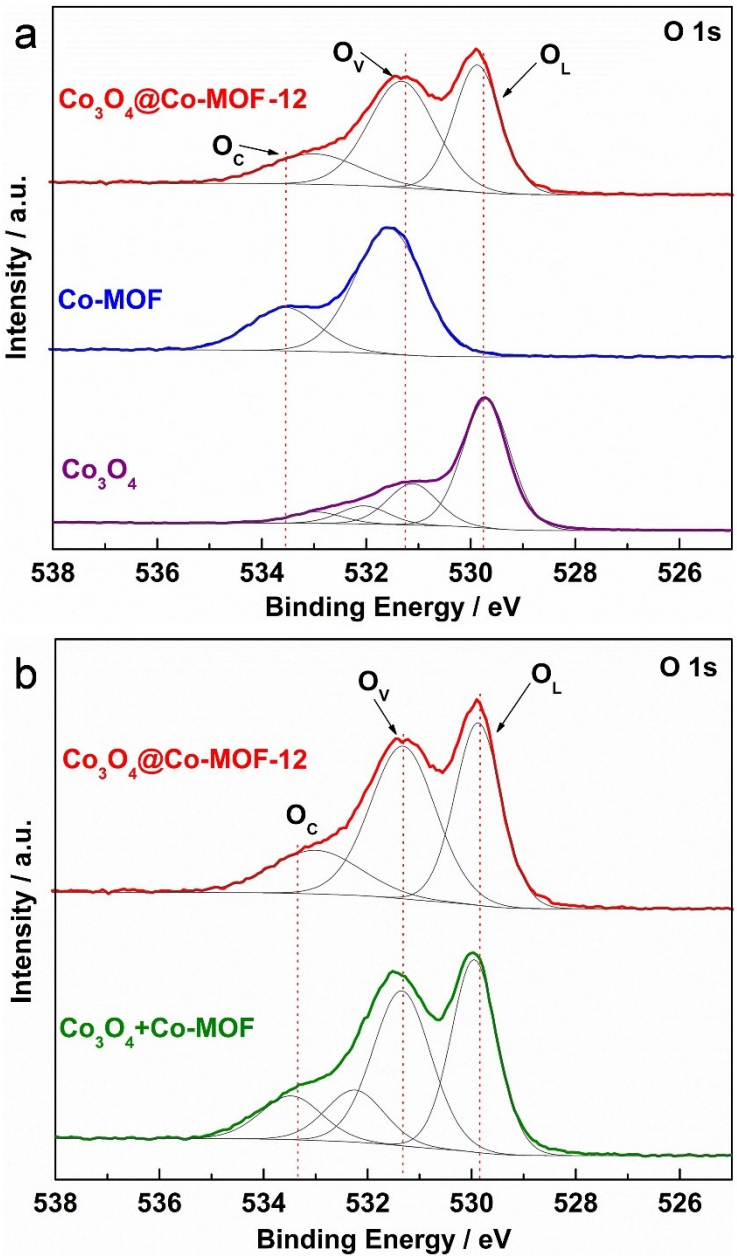

Figure S15. XPS spectra of the O 1s

Figure S15 shows the O 1s XPS spectra, which could be fit with three peaks at 529.7, 531.2, and 533.4 eV, ascribing to the lattice oxygen (O_L), oxygen vacancy (O_V) and chemisorbed oxygen species (O_C), respectively. Furthermore, the O_L peaks of Co_3O_4, Co_3O_4+Co-MOF and Co_3O_4@Co-MOF-12 are also observed, which means that Co_3O_4 existed in this system.

18. BET

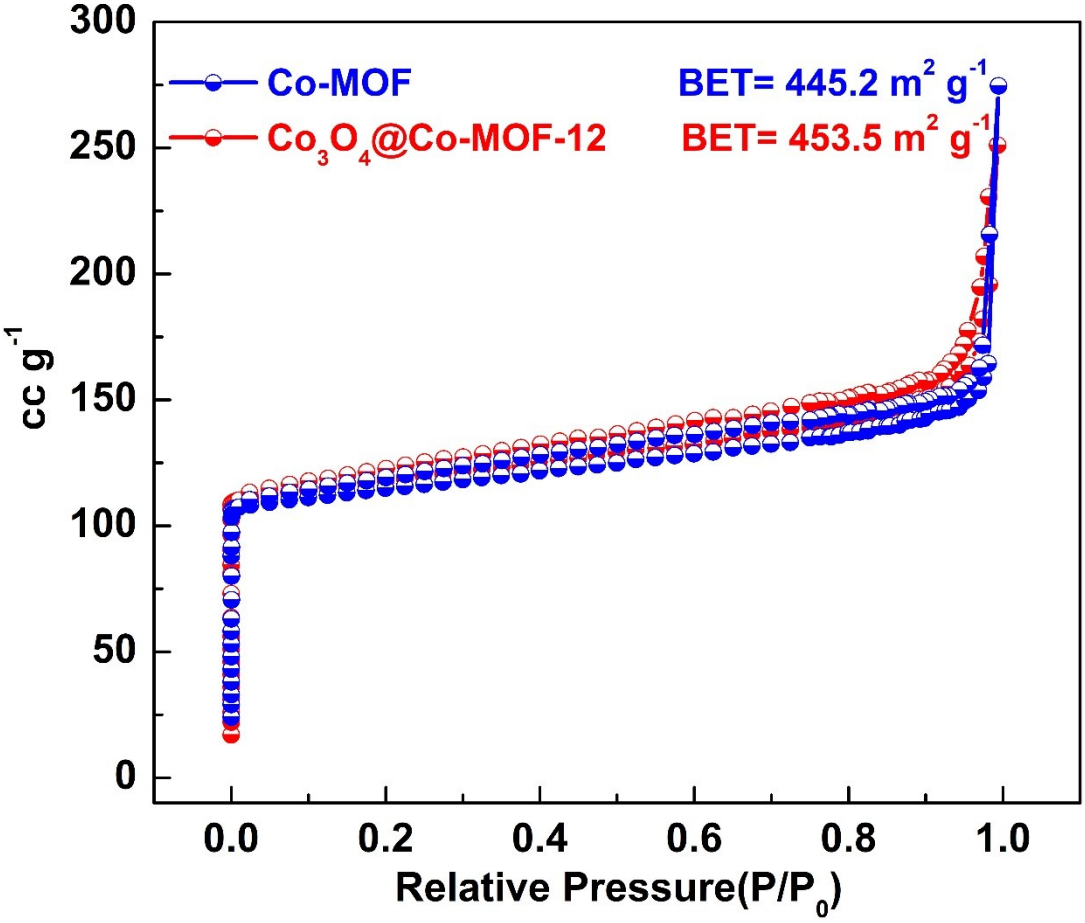

Figure S16. N_2 adsorption-desorption isotherm of the Co-MOF and Co_3O_4@Co-MOF-12.

19. Pore size distribution

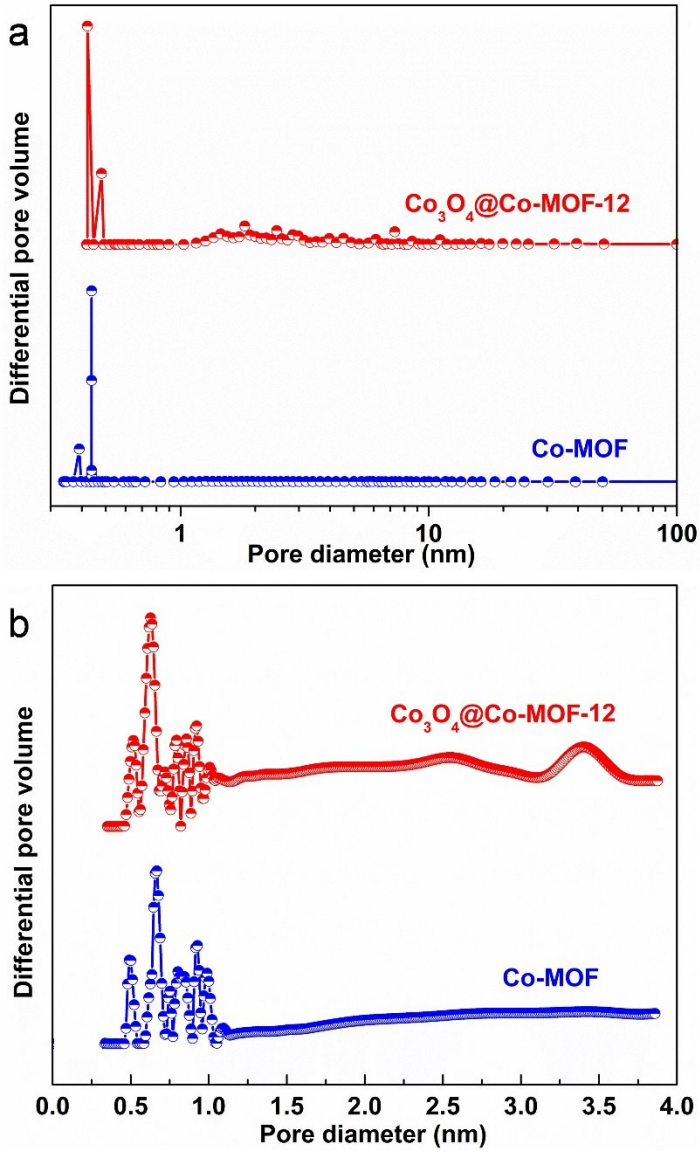

Figure S17. The pore size distribution of the Co-MOF and Co_3O_4@Co-MOF-12 for the BJH adsorption branch (a) and SF method (b), showing the co-existence of micropores and mesopores in the Co-MOF and Co_3O_4@Co-MOF-12.

As shown in **Figure S17**, the pore size distribution for the Barrett-Joyner-Halenda (BJH) adsorption branch implies that the mesopores of the samples are below 20 nm. Furthermore, the pore size distribution was calculated through the Saito-Foley (SF) method and indicated that the micropores were centered at 0.5-1 nm. These results clearly indicate the coexistence of micropores and mesopores in the samples. Therefore, the samples have a high specific surface area.

20. The LSV curves of the Co_3O_4@Co-MOF-12 before and after iR corrections

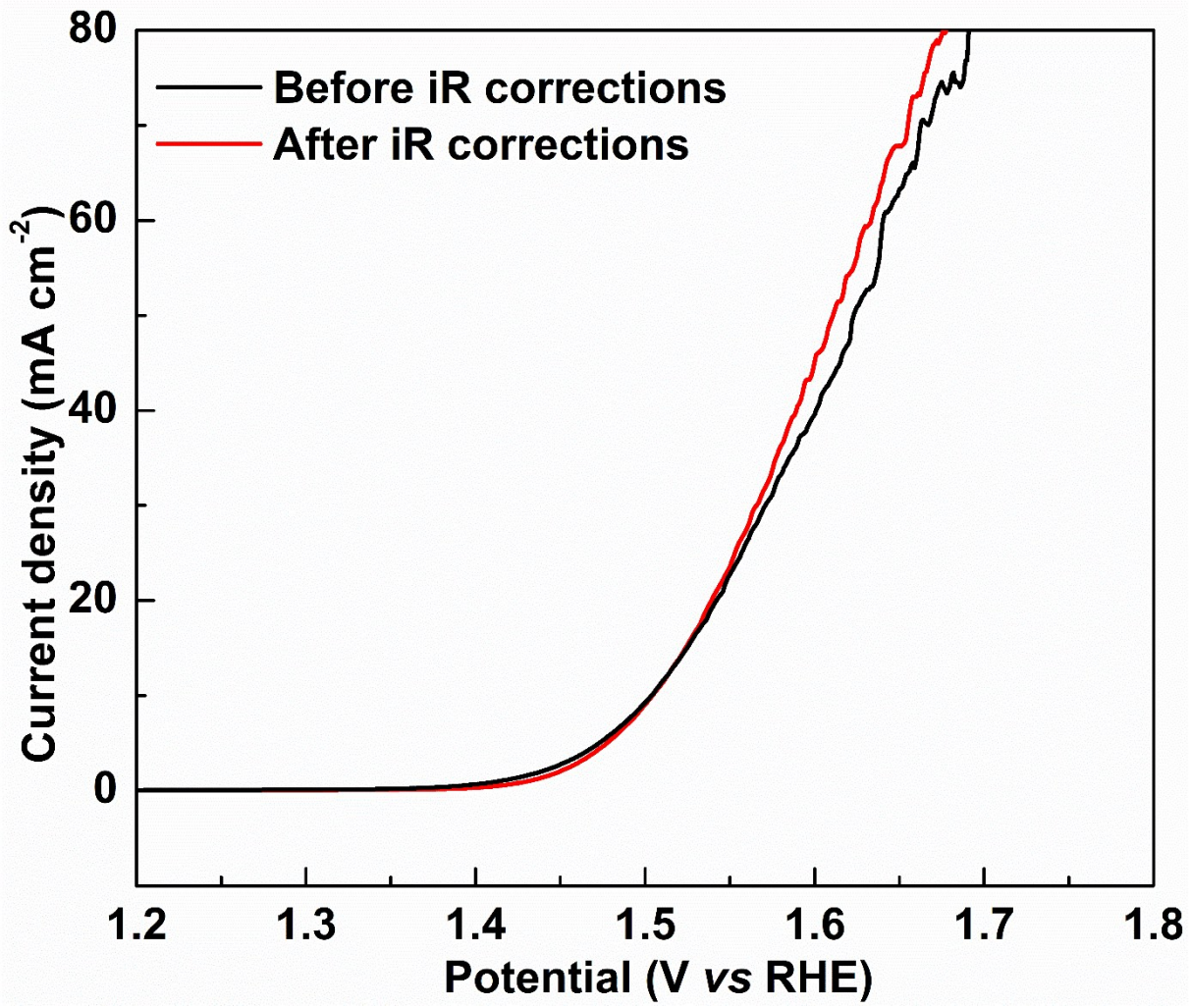

Figure S18. The LSV curves of the Co_3O_4@Co-MOF-12 before and after iR corrections.

21. OER performance of RuO_2 and Co_3O_4@Co-MOF-t

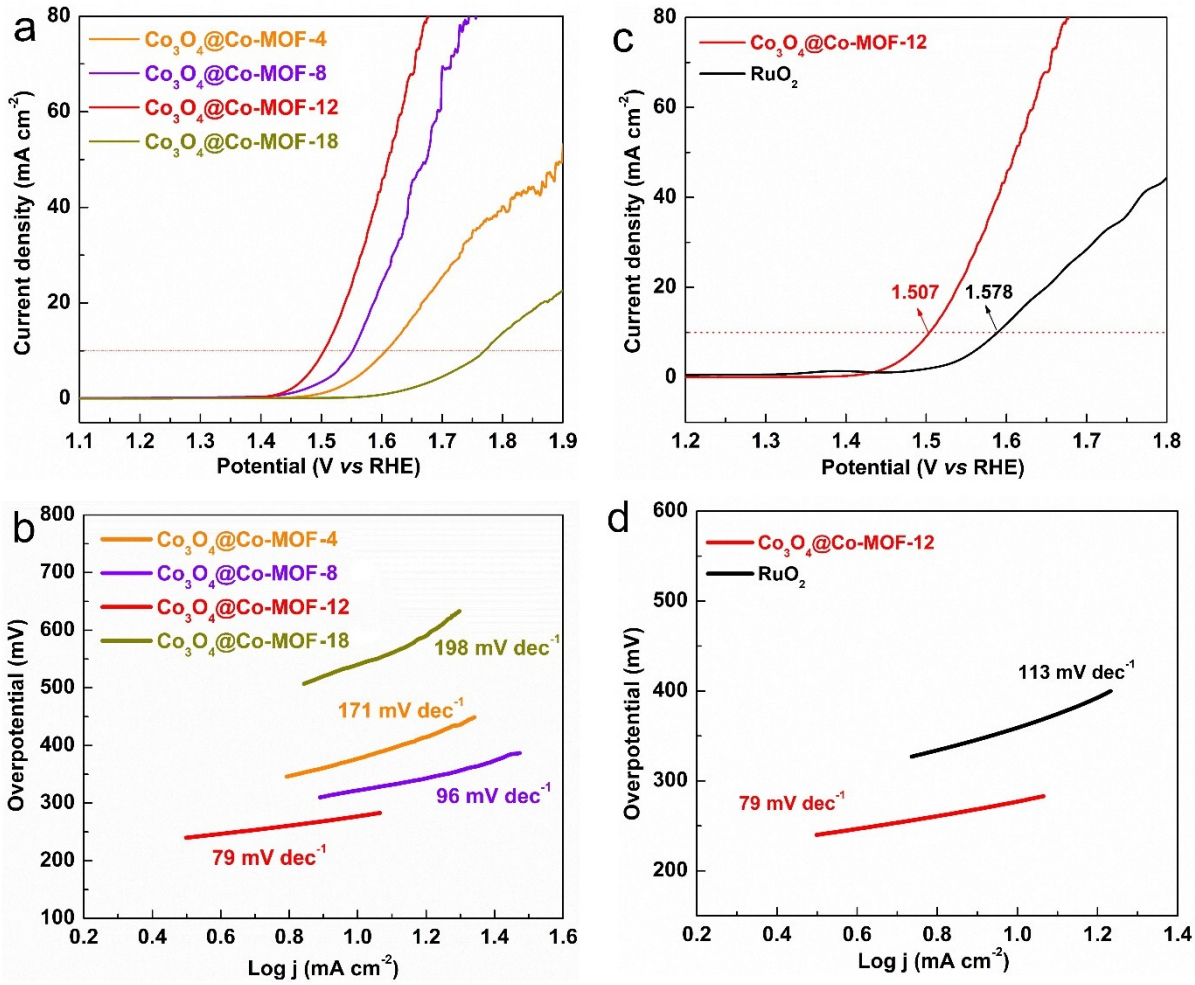

Figure S19. OER performance of RuO_2 and Co_3O_4@Co-MOF-t: a) LSV curves and b) the corresponding Tafel plots of Co_3O_4@Co-MOF-4, Co_3O_4@Co-MOF-8, Co_3O_4@Co-MOF-12, and Co_3O_4@Co-MOF-18. c) LSV curves and d) the corresponding Tafel plots of RuO_2 and Co_3O_4@Co-MOF-12.

22. CV curves

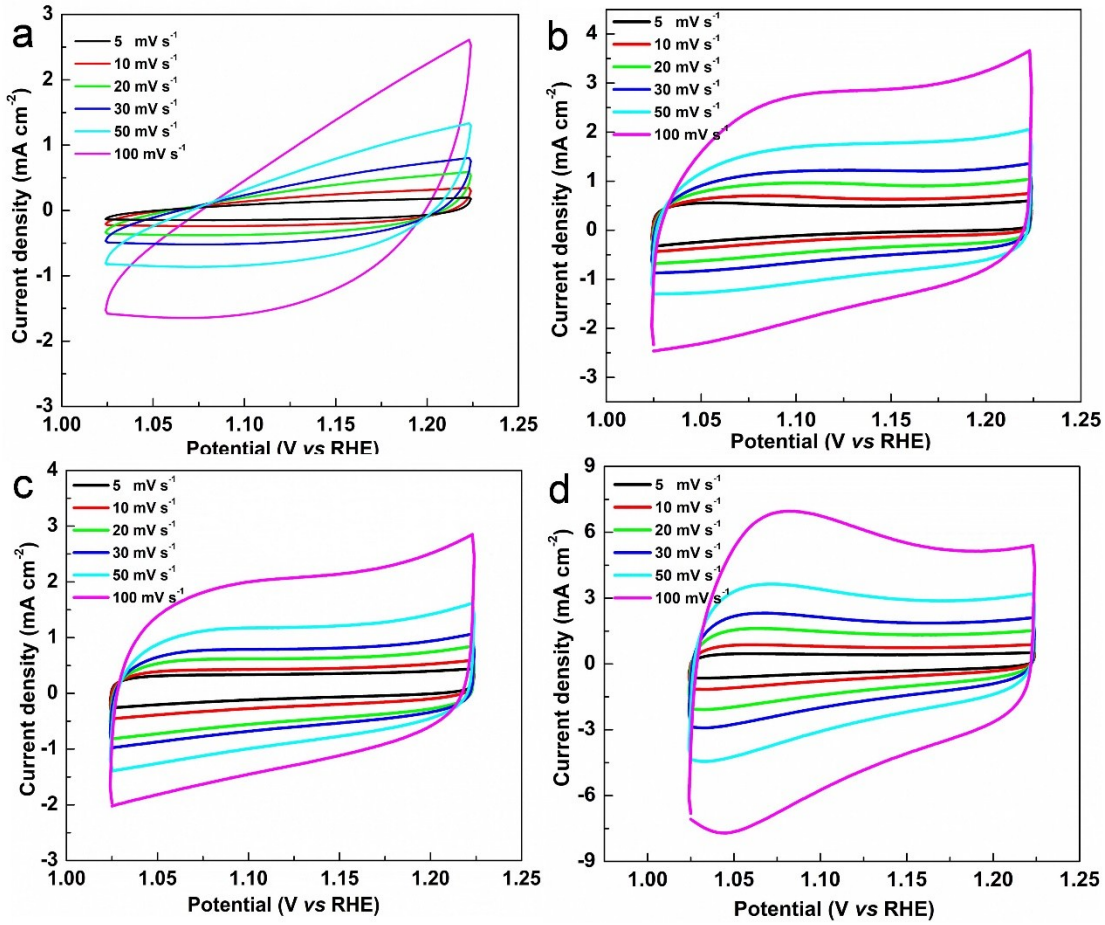

Figure S20. Electrochemical capacitance measurements: CV curves of (a) Co_3O_4, (b) Co-MOF, (c) Co_3O_4+Co-MOF, and (d) Co_3O_4@Co-MOF-12 at scan rates from 5 to 100 mV s^{-1}.

23. The electrochemical impedance spectra of Co_3O_4@Co-MOF for different times

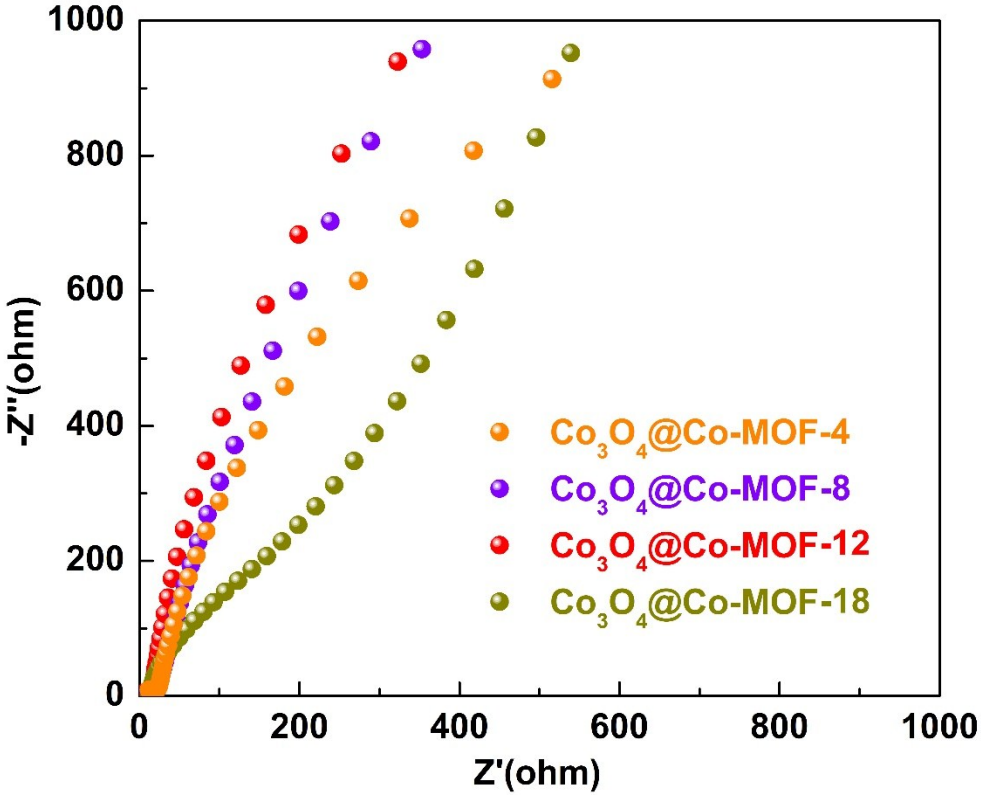

Figure S21. The electrochemical impedance spectra of Co_3O_4@Co-MOF for different times.

24. The electrochemical impedance spectra

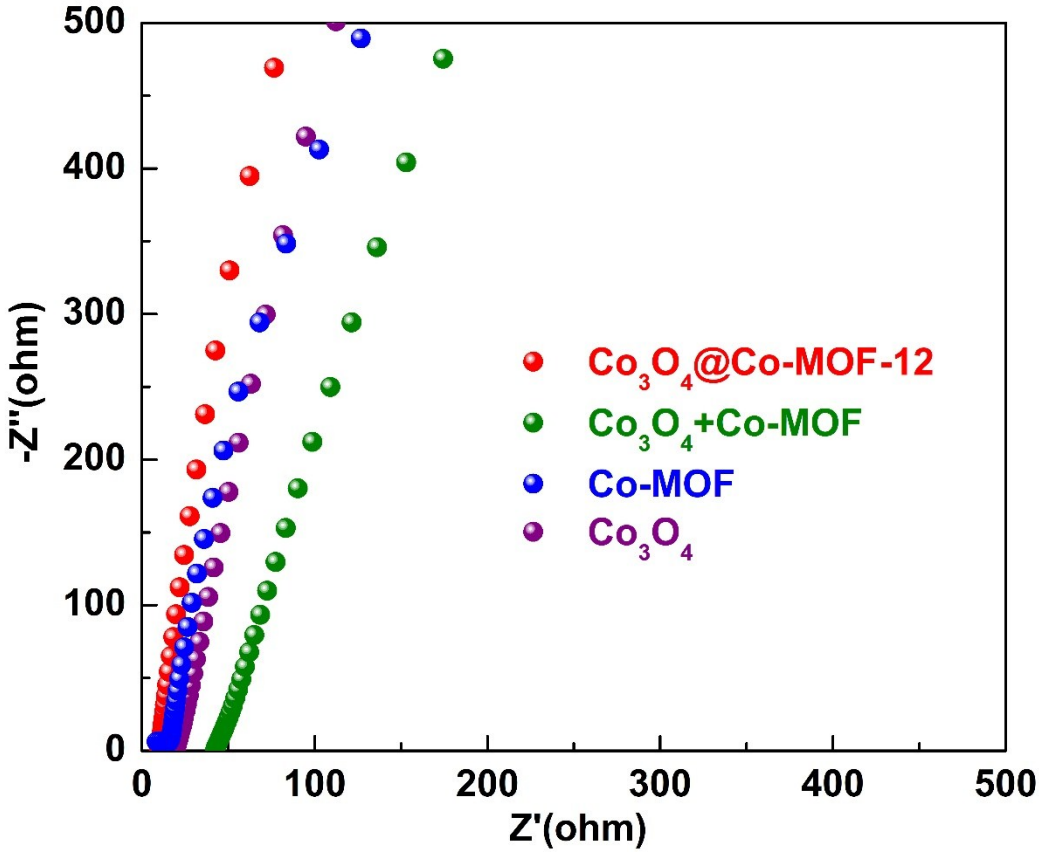

Figure S22. The electrochemical impedance spectra of Co_3O_4, Co-MOF, Co_3O_4+Co-MOF, and Co_3O_4@Co-MOF-12.

25. The electrochemical impedance spectra before and after cycling

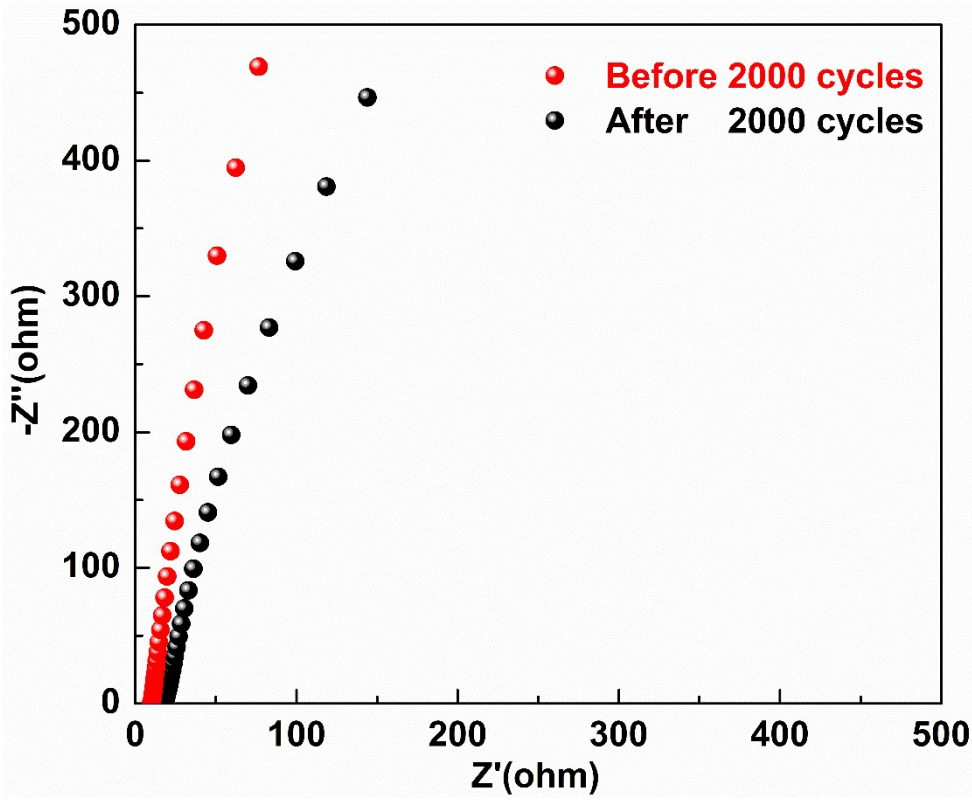

Figure S23. The electrochemical impedance spectra of Co_3O_4@Co-MOF-12 before and after cycling for 2000 cycles.

26. HER

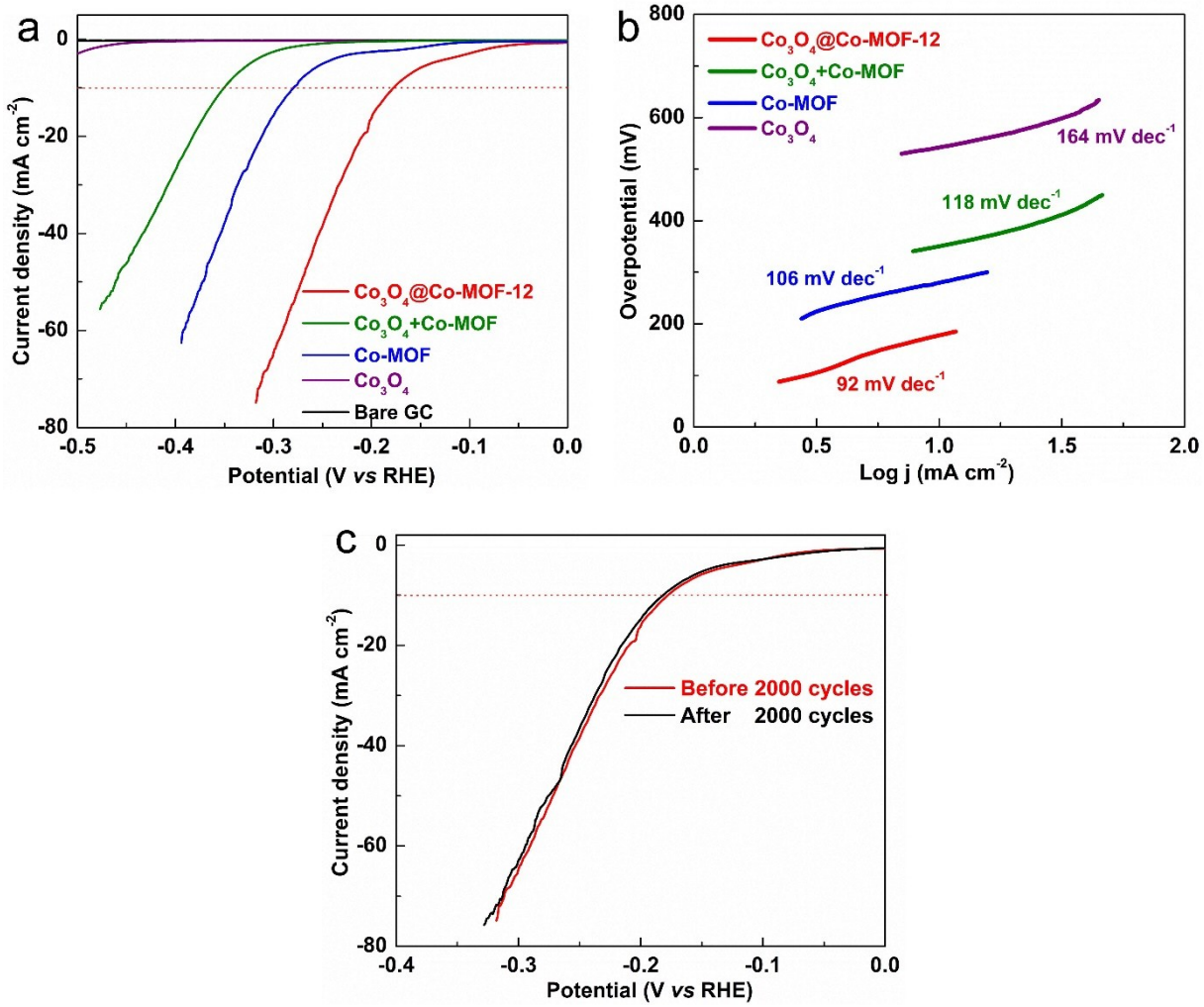

Figure S24. HER performance: a) LSV curves and b) the corresponding Tafel plots of Co_3O_4, Co-MOF, Co_3O_4+Co-MOF, and Co_3O_4@Co-MOF-12. c) LSV curves of Co_3O_4@Co-MOF-12 before and after 2000 CV cycles.

27. HER performance of Pt/C and Co_3O_4@Co-MOF-12

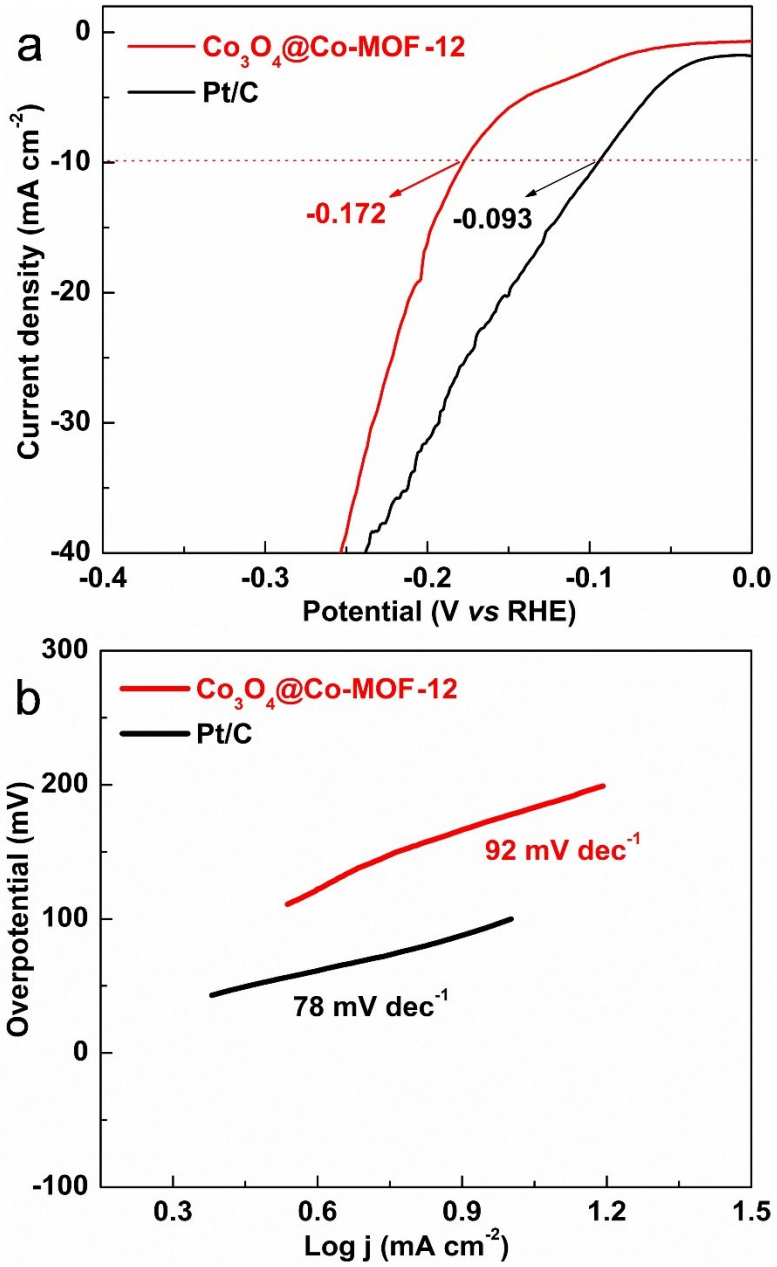

Figure S25. HER performance of Pt/C and Co_3O_4@Co-MOF-12.

28. LSV curves of Co_3O_4@Co-MOF-12 in a two-electrode system

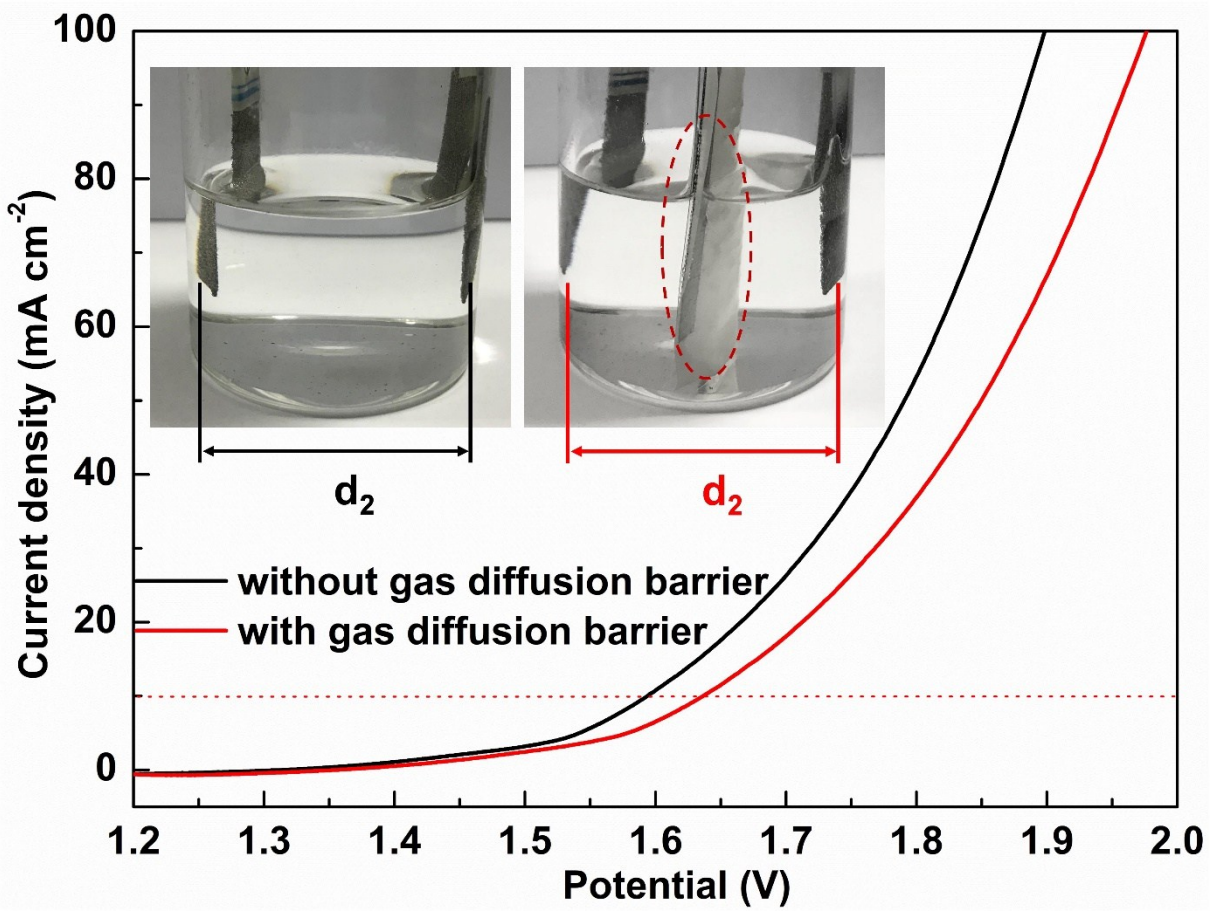

Figure S26. LSV curves of Co_3O_4@Co-MOF-12 with/without gas diffusion barrier at the distance between the two electrodes is d_2.

29. LSV curves of Co_3O_4@Co-MOF-12 in a two-electrode system

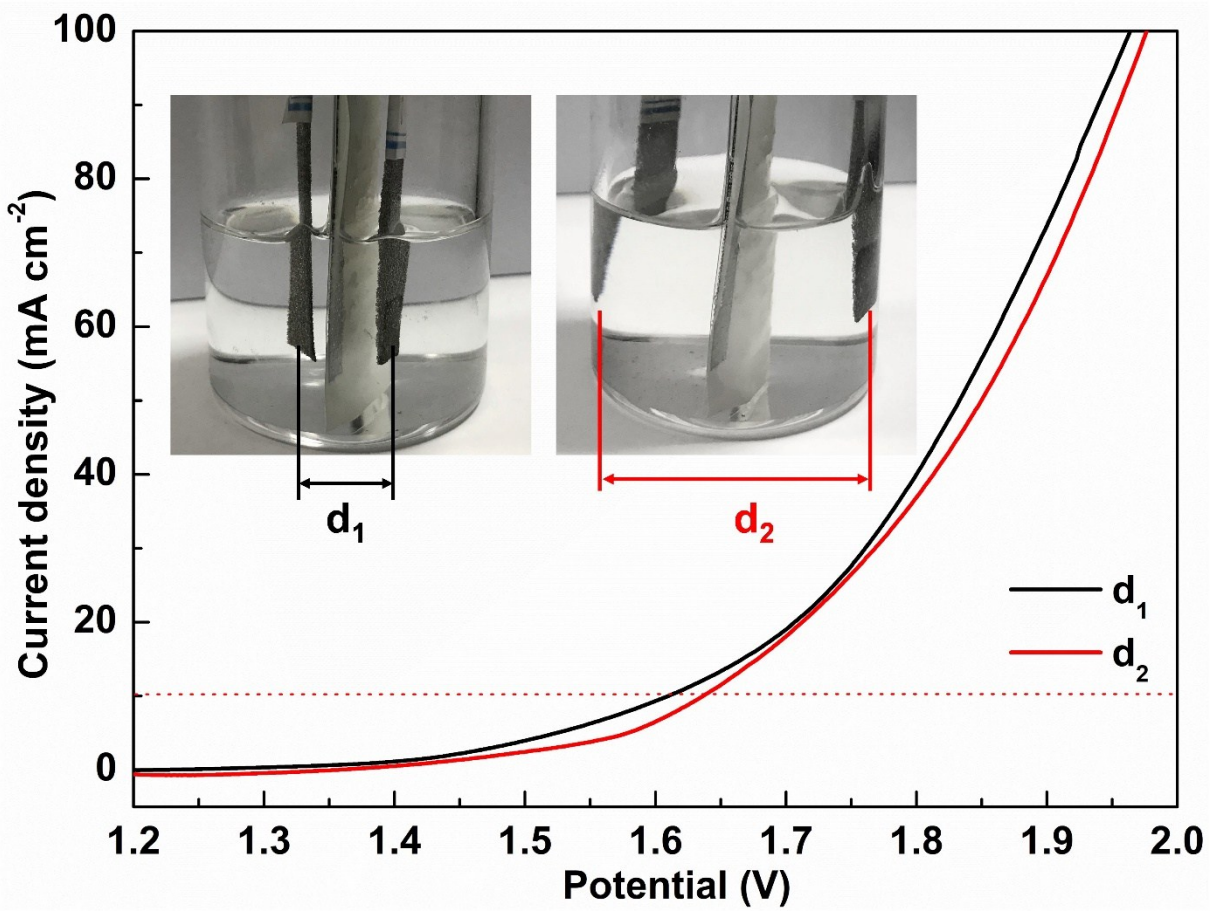

Figure S27. LSV curves of Co_3O_4@Co-MOF-12 with gas diffusion barrier at different two electrode spacing (d_2>d_1).

30. LSV curves of Co_3O_4@Co-MOF-12 in a three-electrode system.

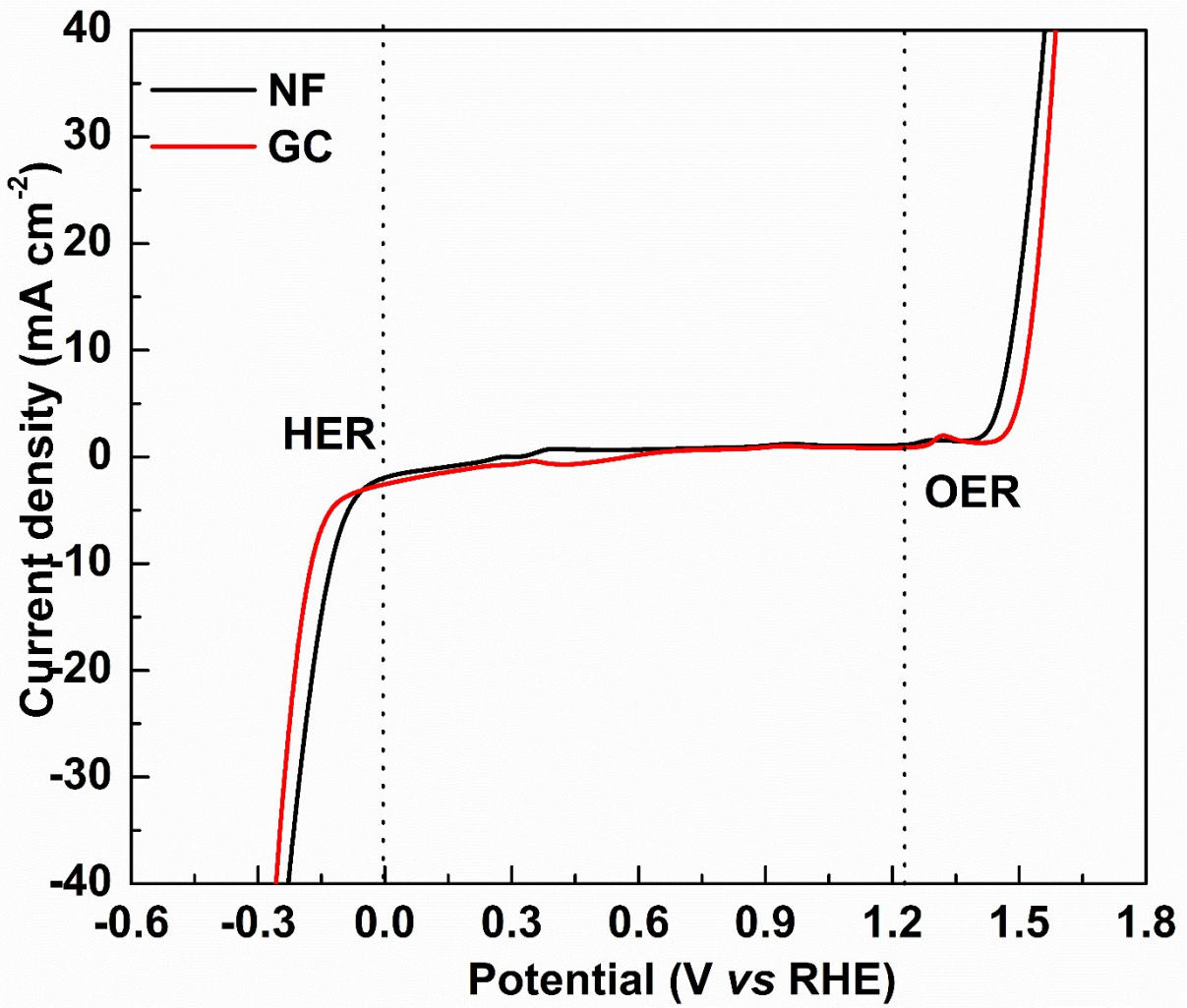

Figure S28. LSV curves of Co_3O_4@Co-MOF-12 based on NF and GC in a three-electrode system.

31. Comparison of the OER activities of Co_3O_4@Co-MOF-12 and recently reported active catalysts

Table S1 Comparison of the OER activities of as-prepared Co_3O_4@Co-MOF-12 and recently reported active catalysts.

Samples	Electrolytes	Overpotential at 10 mA cm^{-2} (mV vs. RHE)	Tafel slope (mV dec^{-1})	Substrate	Binder	Ref.
CUMSs-ZIF-67	1 M KOH	320	53.7	GC	Nafion	1
CoO_x-ZIF	1 M KOH	318	70.3	GC	Nafon	2
Co-NGC@NC	0.1 M KOH	340	91	GC	Nafion	3
Fe_3-Co_2-MOF	pH = 13	283	43	GC	Nafion	4
Co-doped NH_2-MIL-53(Fe)	0.1 M KOH	390	72.9	GC	Nafion	5
MAF-X27-OH	0.1 M KOH	461	66	GC	Nafion	6
NiFeLDH/CNT	1 M KOH	308	35	GC	Nafion	7
ZIF-67@NPC-2	0.1 M KOH	410	114	GC	Nafion	8
CoMn-LDH	1 M KOH	350	43	GC	—	9
Co_3O_4@CoO	pH = 13.6	430	89	GC	—	10
Co_3O_4@Co-MOF-12	1 M KOH	277	79	GC	Nafion	This work

32. Comparison of the overall water splitting performances of Co_3O_4@Co-MOF-12 and recently reported active catalysts

Table S2 Comparison of the overall water splitting performances of as-prepared Co_3O_4@Co-MOF-12 and recently reported active catalysts.

Samples	Electrolytes	HER		OER		Full Cell		Ref.
		η (mV@10 mA cm^{-2})	Tafel slope (mV dec^{-1})	η (mV@10 mA cm^{-2})	Tafel slope (mV dec^{-1})	three-electrode Potential (V@10 mA cm^{-2})	two-electrode Potential (V@10 mA cm^{-2})	
$Co(OH)_2$@NCNTs	1 M KOH	170	—	270	72	1.67/NF	1.72/NF	11
$FeSe_2$	1 M KOH	178	—	245	—	1.653/NF	1.73/NF	12
Co_1Mn_1CH	1 M KOH	180	—	294@30	—	—	1.68/NF	13
Fe-Ni@NC-CNTs	1 M KOH	202	—	274	—	1.706/NF	1.7/NF	14
S-$NiFe_2O_4$	1 M KOH	138	61.3	267	36.7	1.635/NF	1.65/NF	15
MoS_2-Ni_3S_2 HNRs	1 M KOH	98	72	200	—	1.577/NF	1.5/NF	16
ONPPGC/OCC	1 M KOH	446	154	420	84	2.096/CC	1.66/CC	17
NiFe-MOF	0.1 M KOH	134	—	240	34	1.604/NF	1.55/NF	18
$NiCo_2S_4$NW	1 M KOH	210	58.9	260	40.1	1.7/NF	1.63/NF	19
(Ni,Co)Se_2-GA	1 M KOH	128	79	320	70	1.678/NF	1.60/NF	20
Co_3O_4@Co-MOF-12	1 M KOH	172	92	277	79	1.679/GC; 1.60/NF	1.637/NF	This work

33. References

1 L. Tao, C. Y. Lin, S. Dou, S. Feng, D. Chen, D. Liu, J. Huo, Z. Xia and S. Wang, *Nano Energy*, 2017, **41**, 417–425.

2 S. Dou, C. L. Dong, Z. Hu, Y. C. Huang, J. L. Chen, L. Tao, D. Yan, D. Chen, S. Shen, S. Chou and S. Wang, *Adv. Funct. Mater.*, 2017, **27**, 1–8.

3 S. Liu, Z. Wang, S. Zhou, F. Yu, M. Yu, C.-Y. Chiang, W. Zhou, J. Zhao and J. Qiu, *Adv. Mater.*, 2017, **29**, 1700874.

4 J.-Q. Shen, P.-Q. Liao, D.-D. Zhou, C.-T. He, J.-X. Wu, W.-X. Zhang, J.-P. Zhang and X.-M. Chen, *J. Am. Chem. Soc.*, 2017, **139**, 1778–1781.

5 Y. Han, J. Zhai, L. Zhang and S. Dong, *Nanoscale*, 2016, **8**, 1033–1039.

6 X. F. Lu, P. Q. Liao, J. W. Wang, J. X. Wu, X. W. Chen, C. T. He, J. P. Zhang, G. R. Li and X. M. Chen, *J. Am. Chem. Soc.*, 2016, **138**, 8336–8339.

7 M. Gong, Y. Li, H. Wang, Y. Liang, J. Z. Wu, J. Zhou, J. Wang, T. Regier, F. Wei and H. Dai, *J. Am. Chem. Soc.*, 2013, **135**, 8452–8455.

8 H. Wang, F. X. Yin, B. H. Chen, X. B. He, P. L. Lv, C. Y. Ye and D. J. Liu, *Appl. Catal. B Environ.*, 2017, **205**, 55–67.

9 F. Song and X. Hu, *J. Am. Chem. Soc.*, 2014, **136**, 16481–16484.

10 C. W. Tung, Y. Y. Hsu, Y. P. Shen, Y. Zheng, T. S. Chan, H. S. Sheu, Y. C. Cheng and H. M. Chen, *Nat. Commun.*, 2015, **6**, 1–9.

11 P. Guo, J. Wu, X.-B. Li, J. Luo, W.-M. Lau, H. Liu, X.-L. Sun and L.-M. Liu, *Nano Energy*, 2018, **47**, 96–104.

12 C. Panda, P. W. Menezes, C. Walter, S. Yao, M. E. Miehlich, V. Gutkin, K. Meyer and M. Driess, *Angew. Chemie Int. Ed.*, 2017, **56**, 10506–10510.

13 T. Tang, W.-J. Jiang, S. Niu, N. Liu, H. Luo, Y.-Y. Chen, S.-F. Jin, F. Gao, L.-J. Wan and J.-S. Hu, *J. Am. Chem. Soc.*, 2017, **139**, 8320–8328.

14 X. Zhao, P. Pachfule, S. Li, J. R. J. Simke, J. Schmidt and A. Thomas, *Angew. Chemie*, 2018, **130**, 9059–9064.

15 J. Liu, D. Zhu, T. Ling, A. Vasileff and S.-Z. Qiao, *Nano Energy*, 2017, **40**, 264–273.

16 Y. Yang, K. Zhang, H. Lin, X. Li, H. C. Chan, L. Yang and Q. Gao, *ACS Catal.*, 2017, **7**, 2357–2366.

17 J. Lai, S. Li, F. Wu, M. Saqib, R. Luque and G. Xu, *Energy Environ. Sci.*, 2016, **9**, 1210–1214.

18 J. Duan, S. Chen and C. Zhao, *Nat. Commun.*, 2017, **8**, 15341.

19 A. Sivanantham, P. Ganesan and S. Shanmugam, *Adv. Funct. Mater.*, 2016, **26**, 4661–4672.

20 X. Xu, H. Liang, F. Ming, Z. Qi, Y. Xie and Z. Wang, *ACS Catal.*, 2017, **7**, 6394–6399.